MaineDOT

Transportation Research Division

Technical Report 16-03

Bridge-in-a-Backpack™

Task 3.2: Investigate Soil-Structure Interaction – Modeling and Experimental Results of Steel Arches

Final Report – January 2016

Technical Report Documentation Page

1. Report No. ME 16-03	2.	3. Recipient's Accession No.	
4. Title and Subtitle Bridge-in-a-Backpack™ Task 3.2: Investigating Soil – Structure Interaction – Modeling and Experimental Results of Steel Arches		5. Report Date July 2015	
		6.	
7. Author(s) Harold J. Walton, Ph.D. Candidate Bill Davids, Ph.D., P.E. Melissa Maynard, Ph.D Keenan Goslin, P.E.		8. Performing Organization Report No.	
9. Performing Organization Name and Address University of Maine – Advanced Structures and Composites Center		10. Project/Task/Work Unit No. Project 17891.00 – Task 3.2	
		11. Contract © or Grant (G) No. Contract # 20111223*2878	
12. Sponsoring Organization Name and Address Maine Department of Transportation		13. Type of Report and Period Covered	
		14. Sponsoring Agency Code	
15. Supplementary Notes			

16. Abstract (Limit 200 words)

This report includes fulfillment of Task 3.2 of a multi-task contract to further enhance concrete filled FRP tubes, or the Bridge in a Backpack. Task 3 is an investigation of soil-structure interaction for the FRP tubes. Task 3.2 is the modeling and experimental results of steel arches.

This report briefly outlines testing procedures, finite element (FE) modeling methods, and compares models with selected experimental results. The full test plan included two, 6.1 m span, half scale CFFT arches and two stiffness-matched steel arch bridges of the same geometry; scaling properties are discussed in a separate report (Walton et al 2015). Results in this report are limited to the two steel bridges. CFFT arches experience significant concrete cracking during service loading, which reduces experimental repeatability. Further, the accurate determination of arch axial force and bending moment from measured strains is difficult. In contrast, the steel arches were designed to remain linear-elastic throughout backfilling and service-level live loading, which allows for accurate determination of arch internal stress resultants from measured strains and comparison with the FE model results. The experimental results and models focus on bending moment, which is typically the critical buried arch bridge design parameter, supplemented with measured deflection and pressure results from testing. Experimental investigation and model results explore three distinct load conditions presented herein: backfilling process, vehicular live load, and ultimate capacity under apex live loading.

17. Document Analysis/Descriptors Arch bridges, concrete filled FRP tubes, soil-structure interaction, Bridge-in-a-Backpack		18. Availability Statement	
19. Security Class (this report)	20. Security Class (this page)	21. No. of Pages 67	22. Price

Project 1023: Research and Development to Advance Buried Composite Bridge Technologies

Task C (Deliverable 2): Selected Results of Scaled Steel Arch Bridges

7/09/2015
Harold J. Walton, Ph.D. Candidate
Bill Davids, Ph.D., P.E., John C. Bridge Professor and Chair of Civil and Environmental
  Engineering
Melissa Maynard, Ph.D., Associate Professor of Civil and Environmental Engineering
Keenan Goslin, P.E., Research Engineering (formerly of the Advanced Structures and
  Composites Center)

University of Maine Advanced Structures and Composites Center and Department of Civil and
Environmental Engineering

Table of Contents

Introduction

The University of Maine has developed a buried composite arch bridge to efficiently utilize fiber reinforced polymers (FRPs) in civil infrastructure (Dagher et al. 2012). FRPs have good tensile strength, a very good strength to weight ratio, and good environmental durability, including when exposed to salt and water. The composite arch bridge system, illustrated in Figure 1, is comprised of three principal elements: concrete filled-FRP tube (CFFT) arches that span in the direction of traffic, an FRP or reinforced concrete deck that spans between the arches, and granular soil backfill covering the system up to the road surface. The composite FRP-concrete member behavior and gains from soil-structure interaction allow for use of small amounts of FRP in structures, thereby reducing installed cost. This technology has been used in the construction of 12 buried bridges with spans ranging from 7 m to 18 m designed in accordance with AASHTO (2014) LRFD design specifications. Investigations of CFFT performance to-date have focused on the structural capacity of CFFT arches as stand-alone components (Dagher et al. 2012), construction loading effects including local wall buckling during concrete filling (Davids et al. 2013), and FRP material durability (Demkowicz 2011).

Figure 1. Field Load Test of a Buried Composite Arch Bridge

Design of the buried CFFT bridges has generally been conservative with regard to contributions from soil-structure interaction. Bridge behavior has typically been modeled by adding decking properties to the arch properties and including soil in the form of nonlinear elastic soil springs, discussed subsequently in more detail. To-date, over a dozen bridges have been designed using this approach. Long-term field monitoring was performed on a CFFT arch bridge constructed in Fitchburg, MA with live load capacity as the controlling design factor (Quinn et al. 2013). Results measured during bridge loading by two dump trucks indicated FRP extreme fiber strain was smaller than 50 microstrain, equivalent to approximately 0.3% of the fiber tensile strain capacity and 5% of the magnitude of seasonal temperature-induced strains (Quinn et al. 2013). Strains that were smaller than expected for the structure illustrate the need for simulations of soil-structure interaction that more fully account for the soil as a structural element.

3

While the buried CFFT arch bridge system motivates the present study, there has been significant research conducted over the past 20 years examining other buried bridges, typically steel plate structures. Large-span steel culverts and box culverts are similar to CFFT arch structures. They often have shallow cover compared to span, making live load distribution significant (Mak et al. 2009), but the high rise of the legs of the arch or culvert can result in higher moments due to backfilling than due to service live load (Vaslestad et al. 2002). In contrast, small culverts are traditionally buried under sufficient soil such that live load can be effectively analyzed as a uniform pressure acting over a 1:1.15 (depth to spread) area where pressure from all wheel loads is applied uniformly over the spread area (AASHTO 2014).

Traditional design methods can produce excessively conservative results when applied to long-span buried arches with shallow cover. In a study of shallow buried box culverts experimental apex moments were lower than typical Swedish and Canadian design moments by a factor of 3 to 4 depending on cover depth (Bayoglu Flener 2010a), and typical design methods did not capture nonlinearity as applied load approached ultimate capacity (Bayoglu Flener, 2009). However, apex dead load moments compared well with the Swedish design method (Bayoglu Flener 2010b). Structures with similar geometry (span, rise, cover depth, base angle of arch) and construction methods (superstructure cast in concrete foundations, soil compacted in lifts) exhibit similar behavior and face some of the same design challenges.

To predict buried bridge response to live and dead loads, many researchers have adopted complex, two-dimensional (Taleb and Moore 1999) or three-dimensional (Moore and Taleb 1999, Petersen et al. 2010, Elshimi et al. 2014), continuum finite-element models that rely on simulating soil plasticity. Two-dimensional models are effective for modeling backfilling loads which are comprised of uniform soil lifts. However, true truck tire pressures are not effectively predicted with 2D models because they do not account for load dissipation in all directions. Additionally, soil-continuum models are computationally expensive and may be of limited utility for design

engineers who analyze many load combinations and load positions to find the most critical loading state for a bridge.

Another option for modeling soil-structure interaction is a soil-spring model, also known as a p-y model, which represents the structure with one-dimensional beam elements and idealizes the soil with a series of one-dimensional axial-only springs. Soil-spring models use less computational time than soil-continuum models, and are simpler to develop. Spring models are commonly used in pile design including programs such as L-Pile (Reese and Wang 2006), FB Multipier (Chung et al 2011), and Lateral Foundation V2.0 (SoilStructure.com 2013).

Recent investigations using soil springs typically related to dynamic models (Gerolymos and Gazetas 2005) or other repetitive models producing pressure-deflection curves for a series of sand properties (Jeong and Seo 2004) where fewer modeled degrees of freedom allows for shorter run time. Soil springs are used to represent pile behavior in stand-alone piles or integral abutment bridges (e.g, Greimann et al 1986). Soil discretized as a single spring per abutment has produced comparable results to two-dimensional continuum models in integral abutment bridge thermal response (Lehane 1999). Other researchers have used multi-spring analysis where a soil continuum is represented by a series of springs (Ates and Canstantinou 2011). Soil springs used in buried pipe buckling analysis producing strengths that mimic findings from the American Iron and Steel Institute (Kang 2008). The variety of applications and geometries that soil springs have been used in indicates that they can be an effective means of discretizing a buried structure while limiting degrees of freedom.

This report briefly outlines testing procedures, finite element (FE) modeling methods, and compares models with selected experimental results. The full test plan included two, 6.1 m span, half scale CFFT arches and two stiffness-matched steel arch bridges of the same geometry; scaling properties are discussed in a separate report (Walton et al 2015). Results in this report are limited to the two steel bridges. CFFT arches experience significant concrete cracking during

service loading, which reduces experimental repeatability. Further, the accurate determination of arch axial force and bending moment from measured strains is difficult. In contrast, the steel arches were designed to remain linear-elastic throughout backfilling and service-level live loading, which allows for accurate determination of arch internal stress resultants from measured strains and comparison with the FE model results. The experimental results and models focus on bending moment, which is typically the critical buried arch bridge design parameter, supplemented with measured deflection and pressure results from testing. Experimental investigation and model results explore three distinct load conditions presented herein: backfilling process, vehicular live load, and ultimate capacity under apex live loading.

Experimental Program

Two buried steel arch bridges were tested indoors at the University of Maine Advanced Structures and Composites Center. Each bridge consisted of three, parallel steel arches with attached decking. The overall test setup is shown in Figure 2. Details of the structure, test rig, instrumentation, and loading protocol follow.
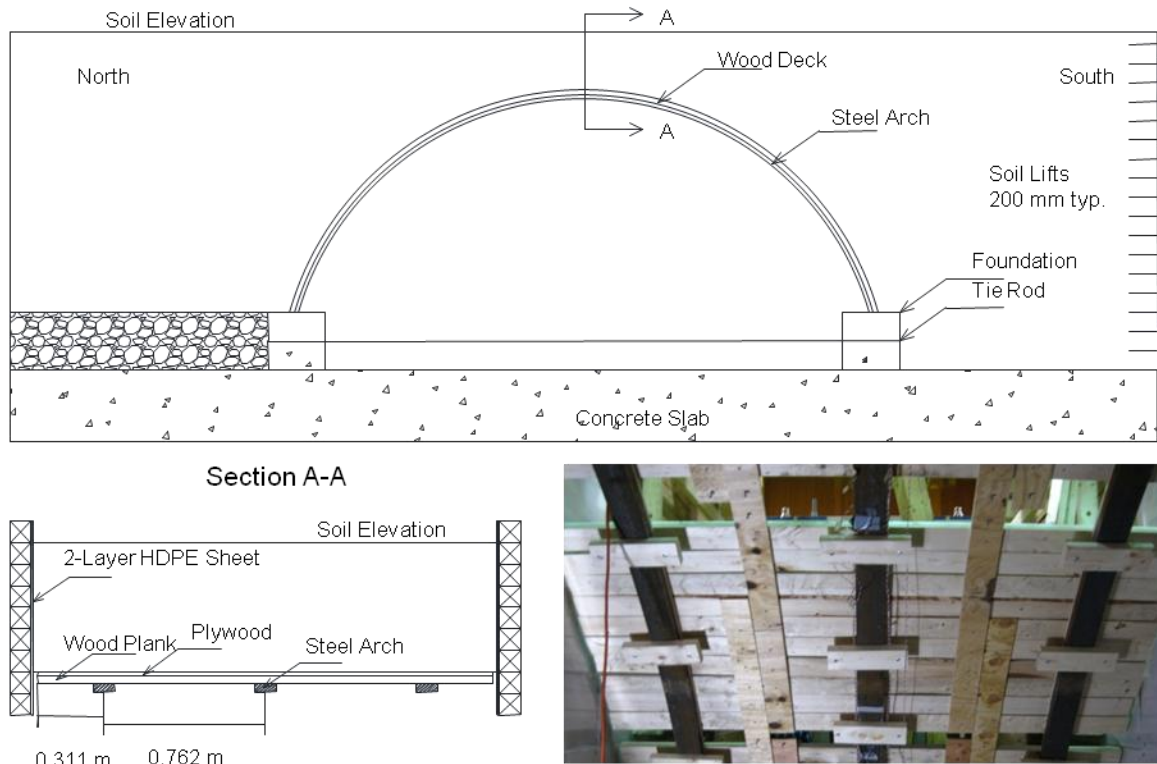
Figure 2. Elevation View of Arches w/Apex Cross Section and Photograph of Decking from

Below Arches During Construction

Soil Confinement Box

Both bridges were constructed on a 900 mm thick concrete strong floor, and contained in a self-reacting heavy timber soil box with inner dimensions of 12.2 m length, 2.2 m width, and 3.7 m depth. The side walls were tied together with 19 mm diameter through rods. Rods passing under the bridge (not in soil) were greater than 150 mm away from the arches to prevent contact during testing. Rods above the bridge (in soil) were greater than 760 mm away from the arches to minimize their effect on soil movement and load shedding. The inside faces of the walls adjacent to the bridge structure were covered in two layers of low-friction HDPE pads to minimize shear stresses between the soil and the box. There was an initial gap of 6 mm to 19 mm between the decking and the walls. Figure 3 is a photograph of the soil confinement box.

Figure 3. Side Elevation View of Soil Confinement Box and Load Frame

Arches

Both structures had three circular-segment profile arches spanning 6.1 m. The tall arches had a 2.29 m rise while the short arches had a 1.22 m rise. To facilitate accurate strain measurement and inference of internal arch forces and moments, the arches were fabricated from grade-50 steel with a mean experimentally determined yield strength of 350 MPa. The arches were solid rectangular cross sections sized to have the same stiffness during service level live loading as CFFT arches having a 2.1 mm thick e-glass shell filled with concrete, design compressive strength of 34.5 MPa, and the same span and rise (Walton et al 2015). The tall steel arch used a 38 mm deep by 102 mm wide rectangular section oriented for weak axis bending and the short steel arch used a 51 mm by 51 mm square section. Arch sections were chosen to ensure a 50% margin of safety against yield during backfilling and service live load. The sections were cold-rolled into an arch shape from bar stock and joined with full-penetration welds to achieve the

required arch length. The arches were cast into geometrically scaled 610 mm x 610 mm x 2130 mm reinforced concrete foundations having a design concrete compressive strength of 24.1 MPa. The arches were embedded 300 mm into the foundations for rotational fixity at the arch-foundation connection.

Boundaries

The bridges were positioned on a thick concrete floor, therefore vertical deflection of the foundations was assumed negligible. In an in-service bridge, the horizontal resistance of the foundation differs depending on the foundation type. Spread foundations provide lateral resistance through basal shear and soil pressure behind the foundation, whereas piles provide horizontal resistance dependent on pile stiffness and *in situ* soil properties. The experiments were designed to bound likely levels of horizontal foundation resistance. Arch foundations were placed on two layers of low-friction HDPE pads, which minimized shear transfer at the foundation-slab interface. The foundations were initially blocked by timbers and wedges to limit inward motion during backfilling. For the initial round of service live load testing, the foundations were tied to each other using steel rods with a total steel area of 1100 mm^2. This made the arches self-reacting, ensured minimal foundation spreading, and represented high horizontal foundation resistance. The rods were initially pre-tensioned, pinning the foundations against the blocking. Subsequent service loading and loading to failure was performed with the tie rods removed to minimize foundation restraint and provide a lower bound on horizontal foundation resistance and capacity of the entire buried structure.

Decking

The three arches were parallel and spaced 762 mm on center. Decking spanned between arches and was cantilevered 311 mm off the centerline of the outside arches. Arch spacing and overhang distance were chosen so the decking would theoretically not rotate at arch locations under a uniform load. Wooden decking was stiffness-matched with a cracked concrete deck on a full-scale bridge and scaled for the models. This is an intermediate stiffness compared to an uncracked concrete deck or an all-FRP deck, both of which have been used for in-service structures. Figure 2 includes a photograph of the tall steel arch in place with decking.

Soil Backfill

Typical CFFT bridges built to date have used well-graded granular fill with less than 10% passing the #200 sieve (i.e., fines) and maximum particle size less than 75 mm. The smaller scale experimental bridges and scaled lift height of 200 mm required a smaller maximum soil size of 25 mm to ensure even spreading and compaction. Soil was classified as AASHTO A-1-a to A-1-b and USCS GP or SP and had an average of 38% gravel (6.4 mm and larger), 61% sand, and 1% fines (passing the #200 sieve). The soil was poorly graded due to a low curvature coefficient related to a smaller upper limit soil size and low percentage of fines.

Maximum dry density determined from the Standard Proctor test (ASTM D698) was 2.05 Mg/m^3 at an optimum moisture content of 6%. Friction angle ranged from 42° to 44° as determined from direct shear testing (ASTM D3080) on dry soil samples having particle sizes greater than 6.4 mm screened out.

During typical bridge backfilling, the soil was compacted with a 9.8 kN vibratory plate compactor, and soil density was measured using the sand cone density method (ASTM D1556). The moisture content for all soil lifts varied between 2.5% and 7%, with over 80% of all

specimens between 3.5% and 4.5%. The average dry density of the compacted material was 2.3 Mg/m^3 with a coefficient of variation (CoV) of 6%. Little variation was found between specimens taken from the center of the soil lift and near the arch sides. The tall bridge was tested a second time with under-compacted soil, as measured densities for compacted bridges were higher than indicated by Standard Proctor test. The loose soil was spread and walked on, but no vibration was applied to the soil. The average density for this soil was 2.04 Mg/m^3 with a CoV of 10%. There was more variation in loose soil density because areas that had been walked on and where soil had been dumped were noticeably denser than soil that was spread and not walked on. Both the compacted and under-compacted soils averaged above the 95% relative compaction requirement based on Standard Proctor density.

The density increase above the Standard Proctor maximum density reflects the benefits of vibratory compaction for granular materials. Visual inspection of Standard Proctor test samples showed looser soil structure than soil compacted inside the soil box. The Standard Proctor test is the benchmark for maximum soil density for the Maine DOT and many other DOTs across the country. However, research by Drnevich et al. (2007) indicates that the Standard Proctor test typically underestimates density for soil with fewer than 15% fines, which is consistent with the soil used for this study.

Instrumentation and Data Collection

Most of the instrumentation was distributed evenly along the arch arc length to best capture results for all loading conditions. Gauges were arranged at the eighth points of the arc length. The numbering scheme referred to throughout this document has gauge locations based on live load position and soil lift order. Each soil lift below the bridge apex was applied individually per side

with the 'South' side receiving a soil lift first and the 'North' side receiving soil secondarily. Gauges start at '0' at the south foundation and end at '8' for the north foundation.

Arch bending and axial strains were monitored with foil strain gauges located at points 0 through 8 of the center arch and at points 0, 4, and 8 for the two outer arches. Strain gauges were arranged in clusters of three per gauge location to measure strains at the top, bottom, and mid-depth of the steel arch section. The middle gauges were difficult to align accurately, and data from them were not used due to questionable reliability. Arch internal moments and axial loads were computed using the top and bottom gauges, the measured steel stress-strain behavior, and the assumption that plane sections remain plane. Apex and foundation moments (locations 0, 4, and 8) are taken as the average of measurements from all three arches. The tall bridge used Vishay 3.2 mm strain gauges, the short bridge used Omega 13 mm strain gauges.

Deflection was measured with 19 gauges for the tall arch and 21 gauges for the short arch. Each arch had the same gauge configuration over the span. Point 4 (apex) vertical deflection was measured on each arch using 130 mm +/- LVDTs. Deflections 2, 3, 5, and 6 in the in-plane horizontal direction were measured using Celesco SP2, 640 mm string pots. Vertical deflection for those points was measured with 80 mm +/- LVDTs. Point 1 and 7 horizontal and vertical deflections were measured with 50 mm +/- LVDTs. The tall arch bridge had two 50 mm +/- LVDTs per foundation located at the mid height of the concrete foundation to measure horizontal foundation deflection. The short bridge had two 50 mm +/- LVDTs near the top of each concrete foundation and two 25 mm +/- LVDTs near the bottom to track foundation deflection and potential rotation.

Soil pressure was measured with Geokon 3500 total pressure cells (TPCs). TPCs were installed while placing the next full lift above the gauge elevation. (For example, a gauge located at an elevation of 900mm was installed with a 1000 mm – 1200 mm soil lift, not the previous lift of 800 mm – 1000 mm.) Horizontal and vertical gauge orientation refers to the direction of

12

measured pressure, e.g. a horizontal gauge has a vertically positioned pressure pan to measure horizontal pressure. Eighteen TPCs were available for each test. After testing the tall arch, the TPC locations were modified for the short arch based on information quality. TPCs near the foundations and the apex had a range of 1 MPa, the other thirteen TPCs had a range of 250 kPa.

The tall arch bridge had two TPCs behind each foundation positioned at mid-height 455 mm from the centerline of the foundation to measure horizontal thrust. All other TPCs were in line with the center of the center arch. Each side of the bridge had a TPC midway between the soil box wall and the foundation measuring horizontal pressure. Positions 1, 2, and 3 had two TPCs to measure horizontal and vertical soil pressures. Positions 4, 5, 6, and 7 had TPCs measuring pressures normal to the arch (for position 4, normal is vertical). Additional TPCs were located in the soil mass mid-way between the arch and the soil box behind points 2 and 6 to measure horizontal pressure. The tall bridge with under-compacted soil had a position 6 horizontal and vertical pressure TPC instead of a normal pressure and rear gauge. All other gauges for the under-compacted test were in the same positions described above for the compacted test.

The short arch had a more symmetric TPC configuration. A TPC measured horizontal pressure behind the center of each foundation and a TPC measured vertical pressure from the centerline top of the foundation. A TPC was midway between the south foundation and the soil box end wall behind the south foundation measuring horizontal pressure. All positions except 4 had a horizontal and vertical pressure TPC. Position 4 had only a vertical pressure TPC.

The zero point for pressure, deflection, and strain is assumed to be the start of backfilling, after arch placement. Data were collected at 1 Hz for all tests, except some backfilling stages for the tall bridge were collected at 0.1 Hz. Instrument noise for all gauges was reduced using a nine-point moving weighted average during post processing. During backfilling, data were collected for the full working day. Backfilling is a multi-day process and the results of subsequent days are appended to the previous results, with the initial values at the start of a day assumed to be the

final values of the prior day. Strains are stored during live loading so that total strains are known during ultimate loading when the arches yield.

Live Load Application

To load each arch as equally as possible, live load was applied vertically using a hydraulic actuator with an HSS8x6x½ spreader beam having dimensions of 152 mm parallel to the bridge span and 2.1 m transverse to the bridge. The initial service load was 41.7 kN, which preliminary FE models indicated produced scaled loads similar to a factored AASHTO (2014) HL-93 tandem. Because of the small magnitude of pressures and deflections measured in the bridge system during initial loading, the service load was doubled to 83.4 kN. For service tests, the load was ramped from a preload of 2.2 kN to the service load over 3 minutes. The 83.4 kN service load was held for 3 minutes, and then the load was ramped down to the 2.2 kN preload over 3 minutes. The load was held at 2.2 kN for typically 1 minute, and this process of loading and unloading was repeated 3 times. During each service live loading event, load effects including arch strains, deflections and soil pressures were locked into the system. Permanent changes due to each individual load application are included when determining total load effects during subsequent load applications. Any creep or relaxation that may have occurred between load steps was neglected because of gauge creep and difficulty reconciling physical changes in the structural system and measurement devices (e.g., zero shift of strain gauges).

Both bridges were initially service loaded at the apex. Load was then applied to alternating sides of the bridge: 1830 mm North, 1830 mm South, 1220 mm North, 1220 mm South, 610 mm North, and 610 mm South, (North and South are relative to the apex; Figure 2). Following this sequence, the apex was then reloaded. Alternate side loading is not a realistic representation of bridge truck loading sequence, but was done to limit permanent side sway throughout the load

sequence. Loading was at even divisions along the middle 60% of the span, and since gauges were placed at even eighth points of the arc length, load and gauge locations do not correspond. The first sequence of service live loading at all locations was performed with the pre-tensioned foundation tie rods in place. The entire service live load sequence was then repeated with the foundation tie rods removed. The tied and untied scenarios bounded both foundation lateral restraint and the horizontal soil resistance developed behind the foundations.

Lastly, the bridge was loaded to failure, defined as irrecoverable loss in carrying capacity, at the apex with the tie rods removed. For the tall bridge, ultimate load was performed by driving the 152 mm wide load beam into the soil until bridge failure. In this case, the load beam embedded 430 mm into the soil, or 70% of the initial cover. For the short bridge a pad made of timbers 100 mm thick, 760 mm in the longitudinal direction, and 2150 mm in the transverse direction was placed over the soil (Figure 4) to mimic pavement on a real structure and prevent punching failure of the load beam above the bridge arch.
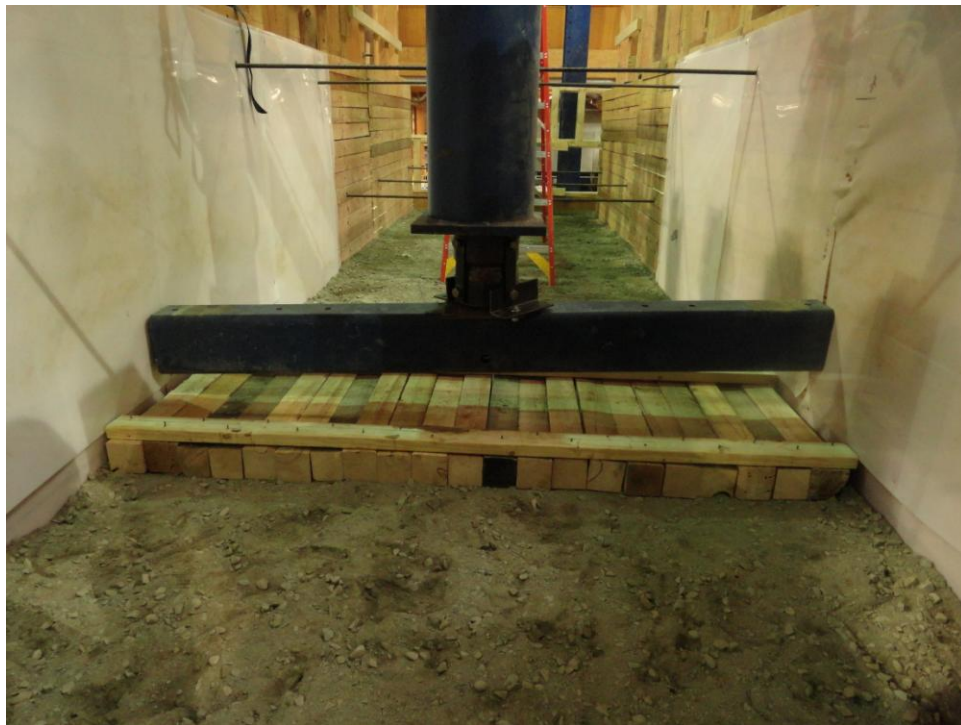
Figure 4. Photograph of Load Beam Before Ultimate Load Test of Short Bridge

Soil-Spring FE Model Description

A single arch is modeled assuming a tributary width of soil equal to arch spacing. This is appropriate for simulating the response of arch bridges in experiments. The arch system is modeled using beam elements, horizontal axial spring elements that represent soil, and very stiff beam and spring elements that represent foundations. These elements are described in detail later. A representation of the model is shown in Figure 5, where a very coarse mesh is displayed for clarity. The arch structure is represented using 2-noded, 2D, Euler beam elements with curvatures defined by cubic shape functions. The arches are given an elastic-plastic response governed by stress-strain behavior (Figure 6) of coupons cut from the same stock used to fabricate the arches and tested in accordance with ASTM A370 (ASTM, 2014). The different experimentally-determined stress-strain properties are used for the models of the tall and short bridges described in the Arches section of this report.
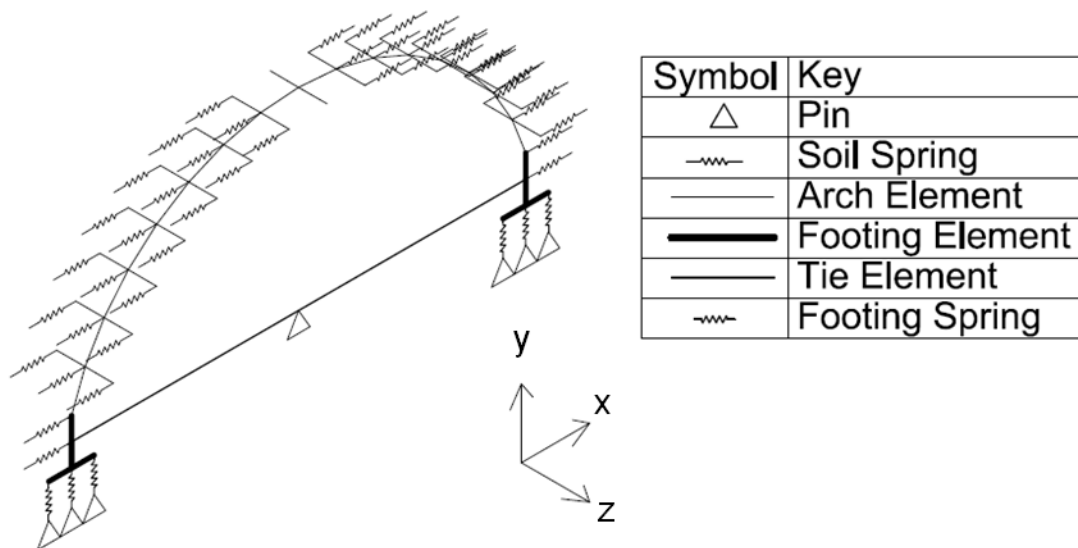
Figure 5. Soil-Spring Model Diagram
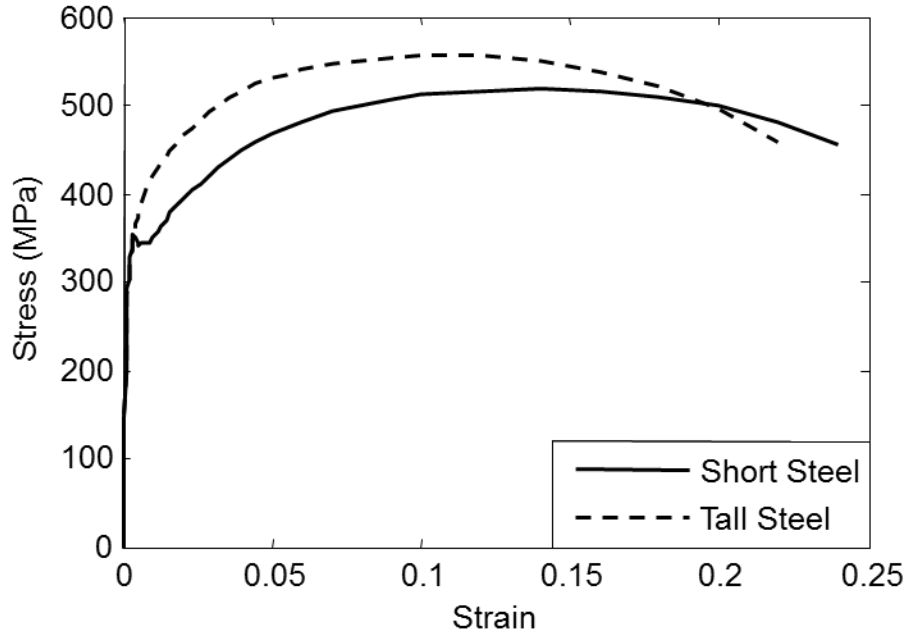
Figure 6. Steel Coupon Stress-Strain

All analyses assume large deformations and small strains under all loadings. Arch loading simulation proceeds in three phases: soil backfilling and self-weight, service live load, and ultimate load. A gravity loaded arch experiences axial compression, and a large deformation solver incorporates the moment created by the axial load acting through the deformation (P-delta effect). Initial simulations for scaling experimental parameters assumed that small deformation analysis was adequate because expected deformations are small (Walton and Davids 2015), but ultimate load simulation showed that P-delta moments were significant. Code was written specifically for simulations reported herein using MATLAB (MATLAB, 2014). A Newton solver is used for backfilling and service live load analysis and a Riks-Wepner solver (Crisfield, 1991) is used for ultimate load analyses, allowing post-buckled response to be predicted. All models used 80 beam elements to discretize the arch, which gave convergent results for all simulations. Model trials indicate a 2% difference in predicted ultimate load between 40 and 80 elements and a 0.2%

17

difference in predicted ultimate load between 80 and 160 elements, indicating 80 arch elements are sufficient.

Simulation of Staged Backfilling

A progressive multi-stage simulation was used to capture the effect of backfilling. In each step, soil depth increases in 200 mm lifts on alternating sides of the bridge apex to mimic construction. With each 'new' lift, vertical loads increase on each arch node below 'new' soil depth. Soil springs are initialized for nodes that are soil-covered during the 'new' lift step. The position predicted for nodes buried during the 'new' lift step defines their at-rest positions and they are given a horizontal earth pressure coefficient of K=1, suitable for compacted soil (Clough and Duncan, 1990). Horizontal spring stiffnesses and lateral earth pressure coefficients for previously established soil springs are iteratively calculated depending on arch displacement and the vertical soil pressure at each node elevation. Details of how soil spring properties were derived are discussed subsequently.

The end of backfilling establishes the baseline locked-in soil stress and soil spring stiffness and arch axial load, moment, and shear appropriate for subsequent live load application. One outcome of sequential backfilling simulations is that soil spring properties and internal arch stresses are not symmetric about the apex prior to live load application. Also, arch stresses are higher during, rather than at the end of, the backfilling sequence.

Application of Live Loads

Following backfilling, loads are applied over the middle 60% of the span at tenth points, corresponding to load points from laboratory experiments. Live load sequence does not matter for the soil-spring model, since all of the elements are elastic springs returning to the original backfill

18

position when live load is removed. Live loads were applied as surface patch loads and distributed through the soil using the Boussinesq assumption (Holtz and Kovacs, 1981). The Boussinesq model assumes load distribution within an infinite half space (infinite length, width, and depth) for a homogeneous, linearly elastic material. Infinite half-space is a reasonable assumption in the span direction, since the experimental soil box is 12.2 m long or 80 times larger than the patch length. In the width direction, the load is applied on 98% of the soil width, appropriately modeled with an infinite strip. Soil is not a homogenous, linear elastic material, however this assumption has traditionally been accepted in design for soil stress below a foundation. Live loading occurs in the model at the top of the soil elevation. This is justified using experimentally observed soil deflections, which were mainly 3% or less of the cover depth based on experimental actuator deflections. The one exception was ultimate loading of the tall bridge, where the load beam punched through 70% of the soil cover depth at failure during the experiment. When simulating this case in the model, live load was applied at 70% below the soil cover depth.

Soil Spring Elements

Soil was modeled as a series of horizontal spring elements connected to an arch node. The soil springs are elastic and are therefore unable to capture the hysteretic load-deformation response caused by soil-arch deformation and relaxation interaction. Soil spring force and stiffness are computed based on the lateral earth pressure coefficient (K), the total vertical pressure (soil and live load), and the tributary area of each spring. The lateral earth pressure coefficient depends on the relative deflection of the arch and the soil height normalized by height from the base of the foundation to the apex of the arch.

The NCHRP (1991) approach for calculating the earth pressure was adopted. The NCHRP (1991) deflection-K curve (Figure 7) uses the traditional Rankine earth pressure coefficients to define ultimate active and passive soil conditions and provides intermediate values based on deflection. Greater soil stiffness correlating to a higher friction angle (ϕ) decreases the deflection required to achieve full active and full passive pressure (Clough and Duncan 1990). For example, dense sand ($\phi = 44°$) requires half as much deflection to achieve the full passive conditions as medium-dense sand ($\phi = 37°$), and loose sands require more deflection than typical granular fills to reach the full passive condition (Figure 7). Compaction modifies the at-rest lateral earth pressure coefficient (K_0). K_0 for a granular soil compacted against a non-moving wall is 1.0 (Clough and Duncan 1990). Following Clough and Duncan (1990), the K-displacement curve is shifted toward a more active state in Figure 7, ensuring a K_0 of 1.0 corresponds to zero deflection.
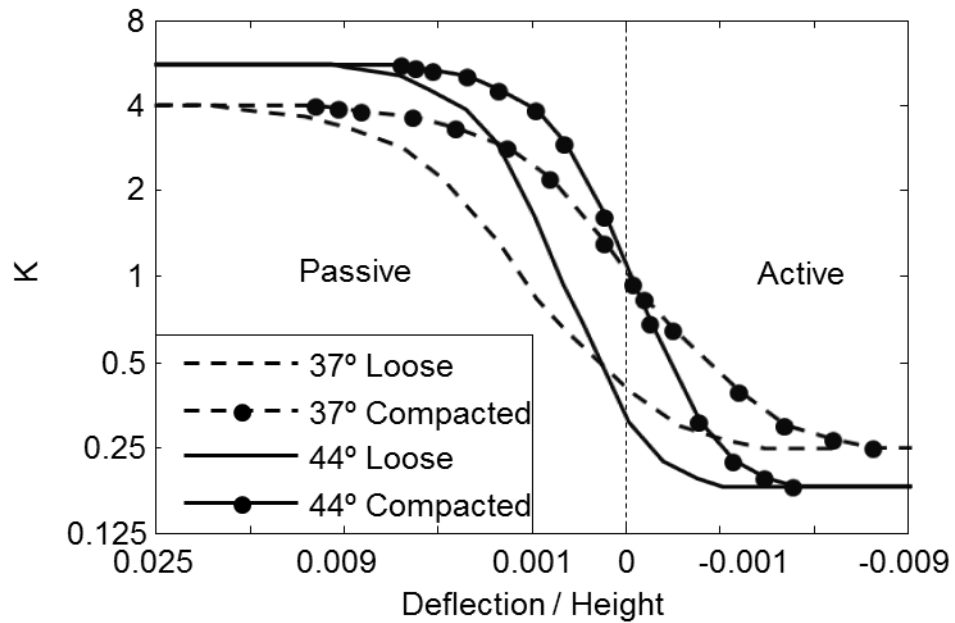
Figure 7. Soil Spring Stiffness Versus Relative Deflection (Reproduced from NCHRP 1991)

The *K*-deflection curve used for the model is based on soil properties from experimental laboratory testing: friction angle is 44° and the total density of the moist soil is 2.4 Mg/m^3. When calculating overburden pressures, pore pressure is assumed to be zero (ignoring positive or suction pressures). Thus, effective stress is assumed to be equal to total stress.

The arch is flexible in a typical backfill simulation, which allows *K* to decrease from the initial compacted value of 1.0. As the arch moves away from the soil during the early stages of backfilling, many soil springs achieve lateral earth pressures that are nearly fully active, regardless of the spring starting point. As soil is added over the apex, its added weight causes the arch shoulders to press into the surrounding compacted soil. The soil springs then compress toward a more passive condition, approaching the K_0 condition. Applied live load causes the arches to sway away from the load. Soil in areas nearest the load experiences more active conditions. As the arch in areas distant from the load is forced into the soil, conditions in the soil move towards the passive region, but remain below the fully passive condition under service-level loads. Only near ultimate load does soil around the arch approach a fully passive condition.

Foundation Elements

Buried CFFT bridge design is currently based on the assumption that the arch is fixed against rotation at the top of the foundation and that the foundation remains fixed in three dimensions. However, experimental results indicate a more realistic representation of foundation response is required, as the toe of the foundation lifted off the floor causing foundation rotation during testing. An assumed pinned base model would not replicate correct motion, as the FE modeled foundation rotates excessively toe downward during backfilling, resulting in an increase in live load moments at the arch-foundation interface. To address foundation rotation, the FE model implemented in this study uses foundations shaped like upside-down tees (Figure 4). Vertical and

21

horizontal foundation beam elements are assigned an elastic modulus typical for concrete and a 610 mm by 760 mm section to ensure they are very stiff compared to the arches. Vertical foundation elements are connected to horizontal soil spring elements and are treated identically to soil springs connected to the arch. The foundation weight is distributed to horizontal foundation elements to resist overturning. The top of the foundation behind the arch is also assigned vertical pressure from the overburden soil. Base foundation elements are supported by vertical nonlinear springs, which have nearly zero stiffness in tension and are very stiff in compression, allowing the toe or heel of the foundation to rotate off the floor, but not penetrate it.

System vertical restraint is entirely controlled by vertical foundation springs. The horizontal spread between the two foundations is initially limited by tie elements given an axial stiffness of 2280 kN/m based on the steel ties described in the Boundaries section. The center of the ties is fixed in the FE model to provide horizontal stability and limit outward horizontal motion before sufficient backfill is applied to each side. Tie elements are assigned nearly zero stiffness during simulation of ultimate and untied service loading to reflect removal of the ties under these loading conditions.

Soil-continuum FE Model Description

Results from the soil-spring model were compared with results from a continuum plasticity finite element analysis using ABAQUS Explicit (ABAQUS 2011) and experimental data. This soil-continuum model is more physics-based than the soil-spring model and implicitly considers soil arching and the bridge geometry when distributing load. In these ABAQUS models, the soil and foundation were modeled using solid elements, while the arch-decking combination was discretized with beam elements.

Model Description

An explicit solver is used for the soil-continuum model because it allows zero stiffness tensile dilation in the granular backfill. Tensile stress develops during backfilling as the top surface of a soil lift bends under self-weight. The tensile stress magnitude is small, but the change in stiffness causes an irreconcilable difference in an implicit solver unless uncharacteristic cohesion is added to the model. However, the explicit solver is expressly dynamic, while the experimental tests performed were quasi-static. Thus, it was necessary to limit the dynamic influence of the model by providing damping and by gradually applying load during dead load and live load steps to eliminate kinetic energy representative of impact forces. All loads are linearly ramped over 1 second of model time and held for one half second of model time in this analysis. Additional ramp time did not appreciably change results but increased computation time.

Each soil lift applied during backfilling is treated as a new analysis. The existing structural and soil states are loaded into the new analysis as a pre-state, with element stresses and deformed mesh geometries caused by the application of all prior lifts retained. The new soil lift mesh geometry is determined from the final nodal locations of the adjoining parts to limit the gap between the parts while insuring no initial overclosure. Geostatic stresses are then applied at the start of the next analysis to the new soil layer. Vertical stress is set to be self-weight and varies over the height of the lift, while horizontal stress depends on the vertical stress and the specified coefficient of lateral earth pressure, K. At the start of a lift, the soil is confined on the bottom surface and the arch surface to prevent dissipation of the soil stresses. The bottom surface of the lift is loaded with the weight of the lift and the arch boundary of the lift is loaded with a combination of the vertical weight and the horizontal pressure, depending on the soil element angle. A graphical representation of the mesh and loading is shown in Figure 8. The confining forces are linearly reduced to zero over the first two-thirds of the next step to gradually initiate

contact between the new lift and the existing elements. The remaining dynamic effects damp out over the last third of the step.
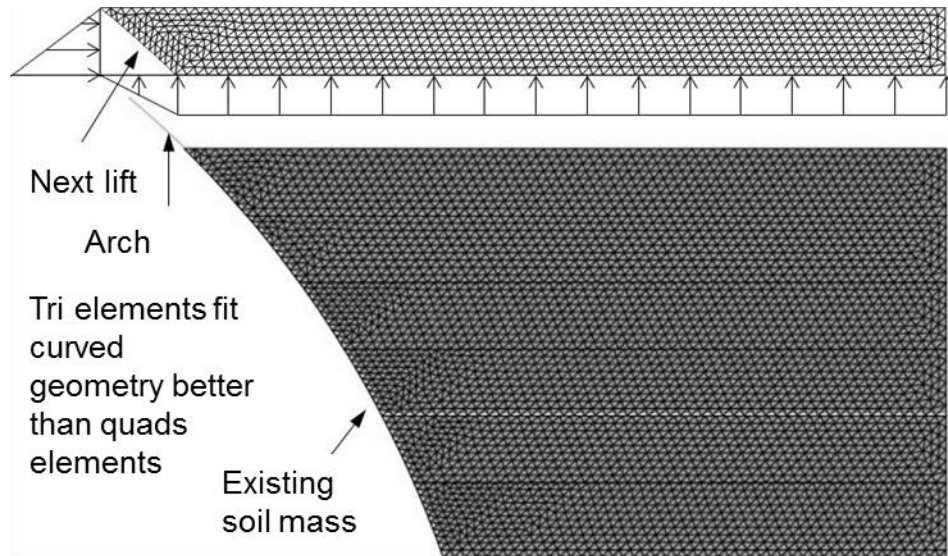

Figure 8. Soil-Continuum Model Lift Placement During Backfilling

Materials

Steel for the arches is modeled using classic metal plasticity, using experimentally determined stress-strain curves presented in Figure 6. An elastic-perfectly plastic Mohr-Coulomb material model is used for the soil, where soil elements have zero stiffness in tension or when the element fails in shear (dependent on stress state, friction angle, and cohesion). NCHRP (2012) indicates that there is a noticeable improvement in load distribution modeling results when using a Mohr-Coulomb model over an elastic model, but there is little value to using a more complicated plasticity model. Mohr-Coulomb plasticity is defined by three parameters: friction angle (ϕ), cohesion, and dilation angle. The soil model also has standard elastic properties and density. To model the soil after experiments, the following parameter values were used: friction angle of 44° (experimentally determined), an arbitrarily small cohesion of 50 Pa, dilation angle of 14° (ϕ − 30° NCHRP (2012)), and total density for compacted granular fill of 2.4 Mg/m^3. An

24

elastic modulus of 28 MPa (reasonable for well compacted granular soil at 1.2 m depth) and Poisson's ratio of 0.3 were assumed after NCHRP (2012).

Other structural components are added to the soil-continuum model based on boundary conditions from experiments. Experiment foundations were tied together and clamped against wooden restraint blocks with steel through ties. The foundations sat on low-friction HDPE pads over a concrete floor that prevented negative vertical deflection, allowed sliding, and did not restrain rotation. The steel ties are modeled with beam elements. All other parts of the experimental foundation system are modeled using plane-stress elements and assumed elastic. Figure 9 shows a detail of the finite-element mesh around the foundation area for a typical model illustrating the range of element types and boundary conditions.
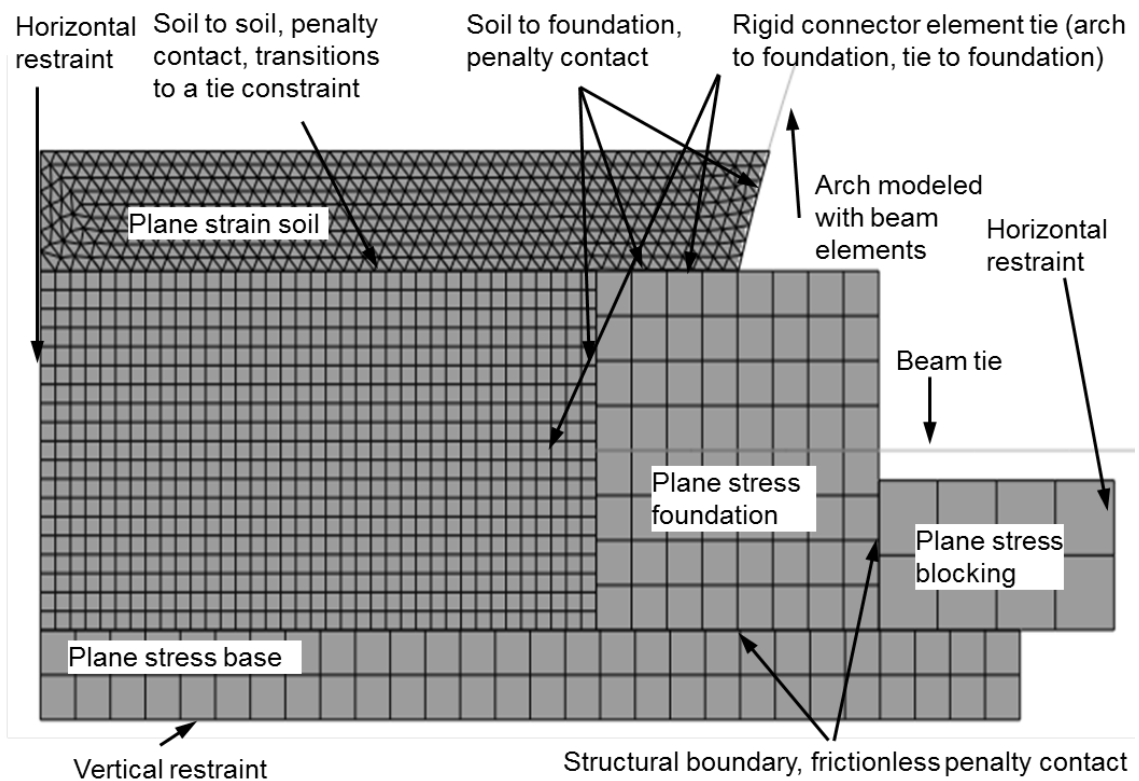
Figure 9. Foundation and Boundary Conditions, Soil-Continuum Model

Contact/Boundaries

The arch and foundation interface and tie and foundation interface are modeled with rigid connector elements. This allows moment transfer between beam and continuum elements. The soil-soil interface between a newly placed lift and soil below is initially modeled as surface-to-surface contact with a rigid normal boundary and a transverse friction coefficient of 0.95, which was large enough to prevent slippage between lifts. Following placement of the lift, this boundary is subsequently changed to a rigid tie so the in-place soil mass acts as one unit. The arch-soil interface is modeled using surface-to-surface contact with hard normal contact and a coefficient of friction of 0.6 (NAVFAC 1986) throughout the analysis.

The vertical soil boundary on the outside of each soil lift is fixed from horizontal movement, but is free to move vertically. Foundation restraint blocks are fixed on their inner edge from horizontal movement and fixed from vertical displacement along the bottom face. The base pads are fixed from horizontal motion along their outer vertical face and are fixed against vertical movement along their bottom face to replicate experiments.

Experimental Results

Backfilling Response

Soil backfilling was performed in lifts, and as is common during construction, lifts were not clearly demarcated. Lifts were delineated while post-processing TPC data to identify TPC vibration caused by the compactor. This allowed data to be presented per lift instead of by time.

The number of backfill lifts differed for each bridge. The short bridge consistently used approximately 200 mm thick lifts with lift 1 being 400 mm on the South side and 200 mm on the North side from the base of the foundation. Lifts alternated by adding 200 mm to each side of the bridge until lift 16. The final three lifts were installed across both sides. The tall bridge initially

26

was backfilled with compacted soil, installed in 150 mm lifts on alternating sides until Lift 14. Lift 1 was 450 mm on the South side and 300 mm on the North side. After Lift 14, soil was installed in 200 mm lifts. Soil lifts alternated until Lift 30, and the final three lifts were across both sides. For the tall bridge backfilled with under-compacted soil, Lift 1 was 600 mm on both the North and South side of the bridge. Lifts were constant soil volume, approximately 1.6 m^3, with average depth 200 mm and installed alternately on each side of the bridge. Soil lifts installed above the apex were also alternating for construction efficiency.

Figure 10 illustrates North foundation soil pressures for the short bridge. Figure 11 illustrates North foundation soil pressures for the tall bridge with under-compacted soil. The tall bridge with compacted soil had soil pressures measured using horizontal TPCs only (not vertical and horizontal TPCs as with the other bridges) and soil pressures are not presented for this structure. Figure 10 and Figure 11 indicate that changes in vertical pressure alternate between large gains, when soil is placed over the given side, and small gains, when soil is placed on the opposite side and the foundation under the gauge rotates. They also indicate that horizontal pressure behind the mid-height of the foundation does not increase uniformly with the addition of each lift. Horizontal pressure increases modestly for the short bridge during the early stages of backfilling, and increases more rapidly during final backfilling stages. This is a sign of horizontal foundation thrust and movement, which can be significant for a short arch structure. Early in backfilling, the soil drives the foundations together. When soil elevation increases, more axial load is carried by the arches. Figure 12 illustrates axial loads computed from measured short arch strains at the North foundation, highlighting this increase in arch compression with increased soil elevation. While some of the horizontal foundation thrust caused by arch axial load is carried by the steel tie rods, some of it also results in higher horizontal soil pressures behind the foundations.
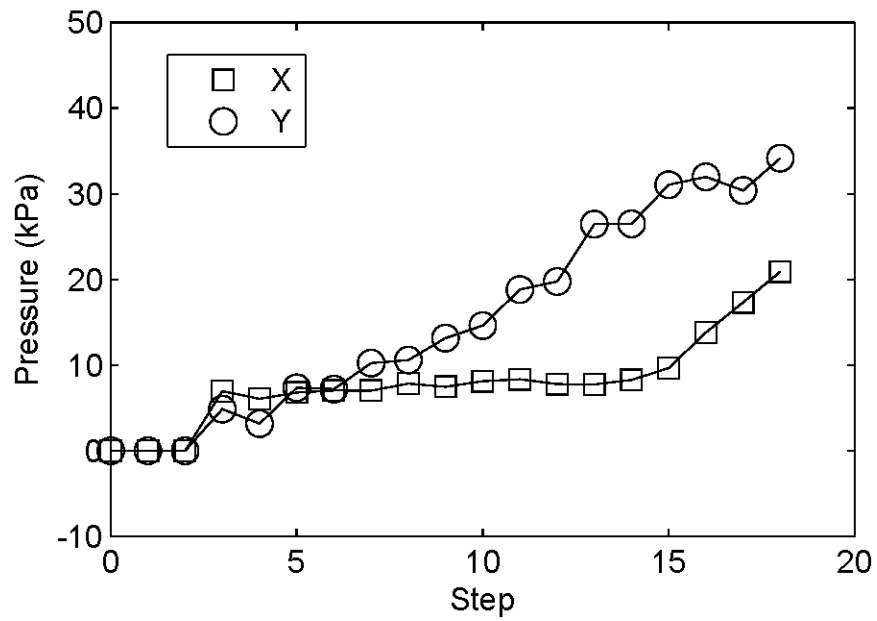
Figure 10. North Foundation Pressure During Backfilling, Short Bridge
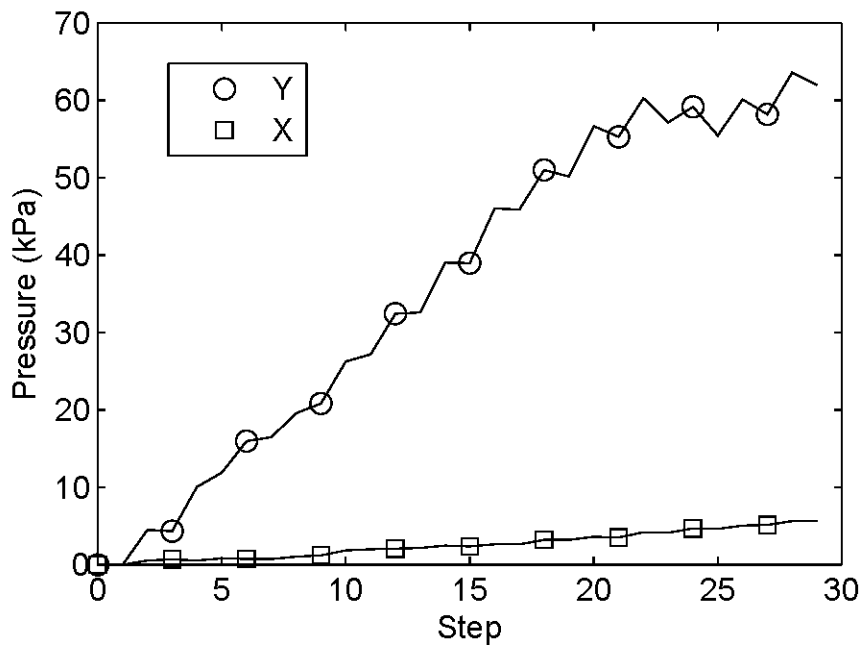

Figure 11. North Foundation Pressure During Backfilling, Tall Bridge, Under-Compacted Soil
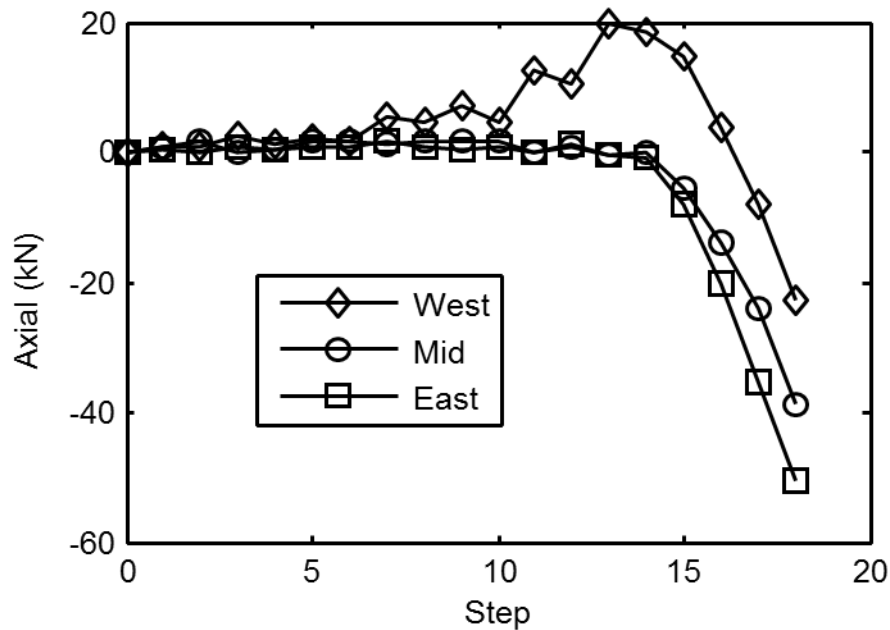
Figure 12. North Foundation Axial Load During Backfilling, Short Bridge

The change in vertical foundation pressure added per lift decreases as backfilling progresses for the short bridge. Early lift pressures increase by an amount equal to or greater than the weight of overburden soil, while later lifts have pressure changes less than the weight of overburden soil. This suggests that foundation rotation during soil placement and high axial loads cause the heel of the foundation (buried in the soil) to dip down while the toe of the foundation rotates upward. In contrast, tall bridge vertical pressure increases remain nearly uniform per lift and closely reflect the weight of overburden soil, indicating little foundation rotation.

Also notable in Figure 12 is that the axial loads in the arches near the foundation are in net tension for the first half of loading. Horizontal force from soil pressure along the arch creates tension in the section while vertical soil force creates compression in the section. Early stages of backfilling have larger horizontal force from compaction than vertical force due to the steep arch angle near the foundation. Soil forces applied above the shoulder are mostly vertical due to arch shape, which results in predominantly compressive axial load. At the same time the horizontal

29

soil forces closer to the foundation become more active as the arch is driven by the soil. The inconsistency in axial load between arches is likely result of from arch geometric irregularity near the footing resulting from manufacturing. Arches were welded to length from pre-bent sections, and when cast in footings, the apex and shoulders of all three arches were aligned. However, this caused the arch-foundation position to vary slightly and resulted in uneven loading in the bottom eighth of the arc length.

Figures 13, 14, and 15 illustrate apex displacements (positive upward) during the backfilling process for the short bridge, the tall bridge with compacted backfill, and the tall bridge with under-compacted backfill, respectively. The short bridge has good agreement between each of the three arches, with a peak displacement near 10 mm and final displacement near 6 mm. The tall bridge has greater apex displacements than the short bridge, with compacted soil peak displacements between 12 mm and 18 mm, and under-compacted soil peak displacements between 24 mm and 30 mm, approximately 0.5% of the height for both compacted bridges and 1% of the height for the under-compacted bridge. Peak displacements for the tall bridge were larger for the under-compacted soil, indicating that denser soil in the compacted bridge provides more restraint to bridge movement, as expected.
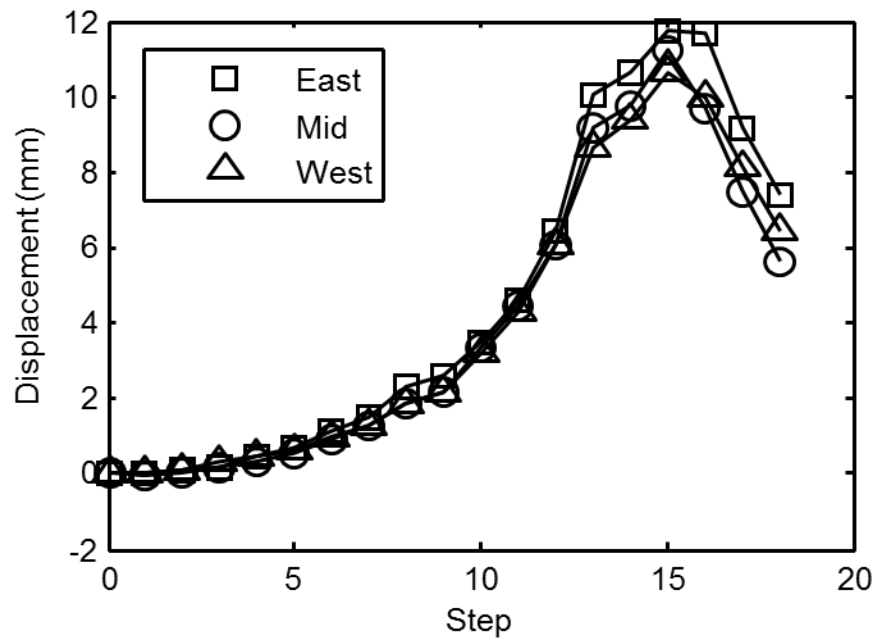
Figure 13. Apex Displacement During Backfilling, Short Bridge
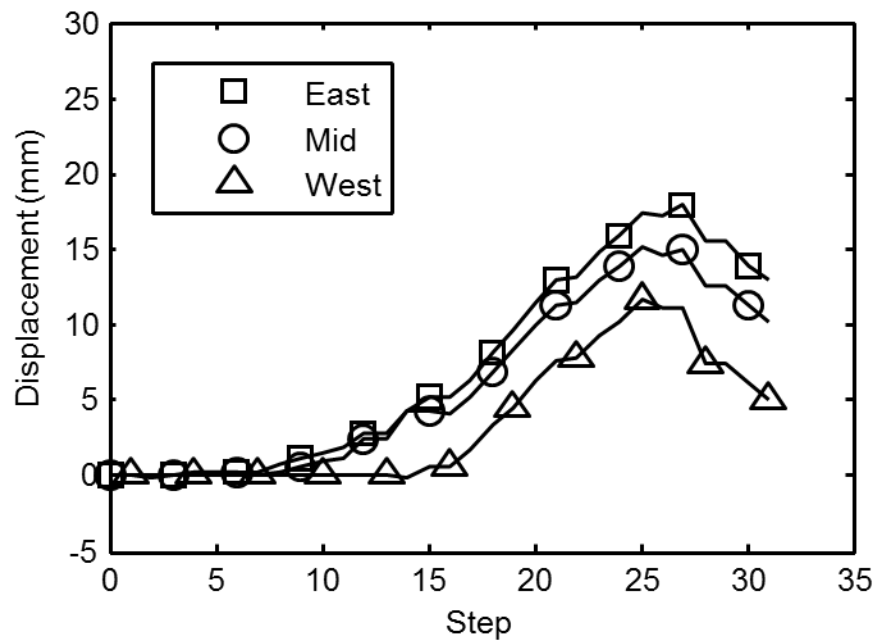
Figure 14. Apex Displacement During Backfilling, Tall Bridge

31
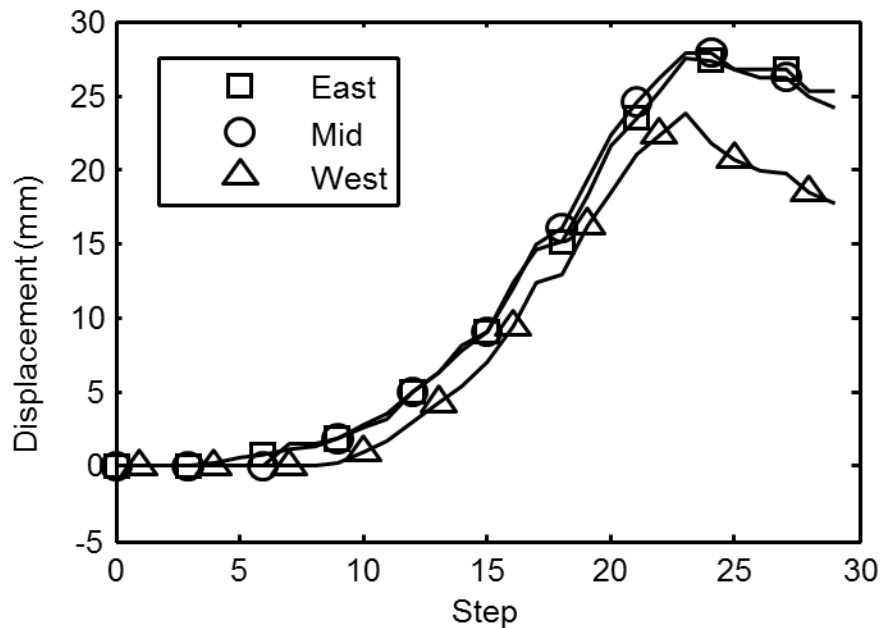
Figure 15. Apex Displacement During Backfilling, Tall Bridge, Under-Compacted Soil

This trend also holds true for arch bending moments inferred from measured strain during backfilling. Figures 16, 17, and 18 contain the moment for the center arch at the foundation, apex, and shoulder throughout backfilling for the short compacted bridge, tall compacted bridge, and tall under-compacted bridge, respectively. There are negative moments at the foundation and apex locations and positive moment at the shoulder for all bridges (positive moment produces compression on the outside face of the arch). The apex moment follows the same shape as the apex deflection and at the end of backfilling becomes less negative. The moments for the tall compacted bridge are lower than for the tall under-compacted bridge. Compacted soil is stiffer due to higher friction angle and lower void ratio and develops greater passive resistance and smaller active loading than under-compacted soil. Despite the greater compaction energy required to achieve a higher as-placed density, the compacted bridge has smaller moment and deflection during backfilling due to soil restraint.
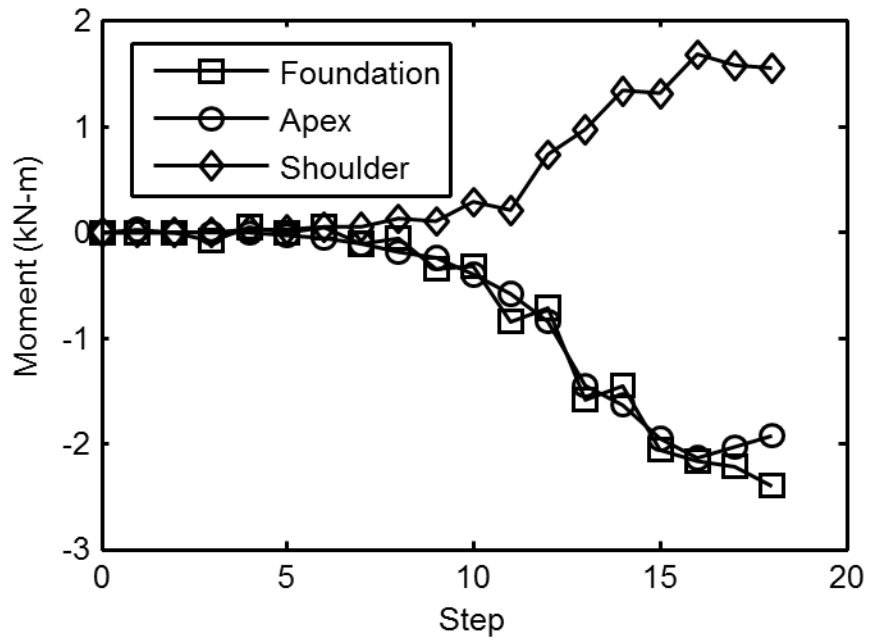
Figure 16. North Side Moments, Middle Arch, Short Bridge
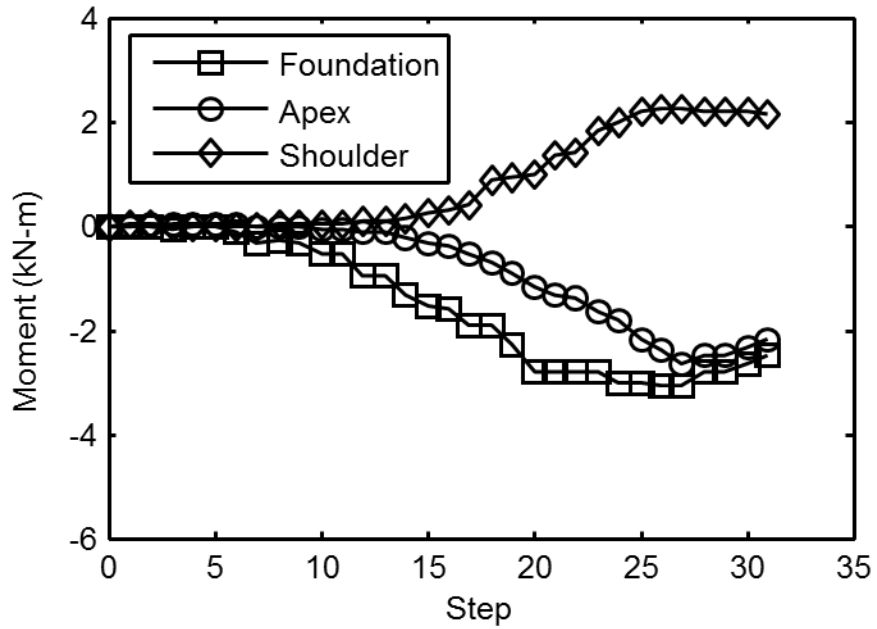
Figure 17. North Side Moments, Middle Arch, Tall Bridge
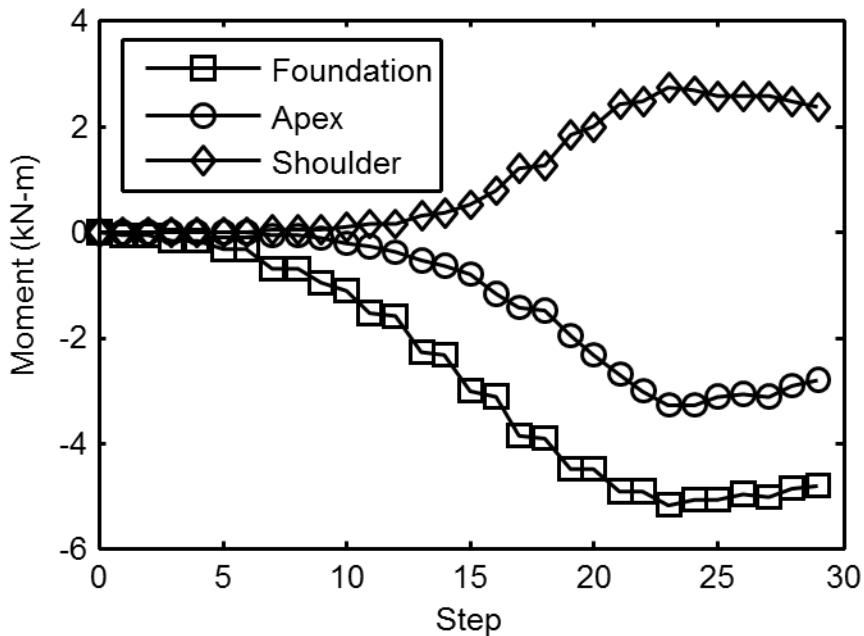
33

Figure 18. North Side Moments, Middle Arch, Tall Bridge, Under-Compacted Soil

Arch moments at the foundation of the tall bridges are higher than either shoulder or apex moments and deserve design consideration. Also, the peak moment occurs prior to the end of backfilling, which indicates that an analysis that ignores the backfilling progress will not find this potential worst-case loading. This finding is consistent with model results of plate steel arches where peak moment occurs when the soil is at or just above the apex (Morrison, 2000). However, the approximate 50% difference in backfilling footing and apex moment between under-compacted and compacted soil disagrees with results for steel plate arches (Webb et al. 1999), which indicated that compaction had little effect on backfill moment.

Figure 19 and Figure 20 show apex moment during backfilling for the tall and short bridges with comparisons to both models. Notice that for the tall bridge, both models have nearly identical results and the experimental peak moment is well predicted by both models. The models have a smaller moment reduction from peak than experimental results. The short bridge apex

moment is not as well represented by either model, and both models are unconservative. The soil-spring model final moment is closer than the soil-continuum model, but the soil-continuum model better follows the trend indicated by experimental results; soil loads above the apex produce positive moment experimentally and in the soil-continuum model, reducing the negative moment from prior loading. The soil-continuum model suggests that the final two lifts approaching the apex, one per side, produce positive apex moment.
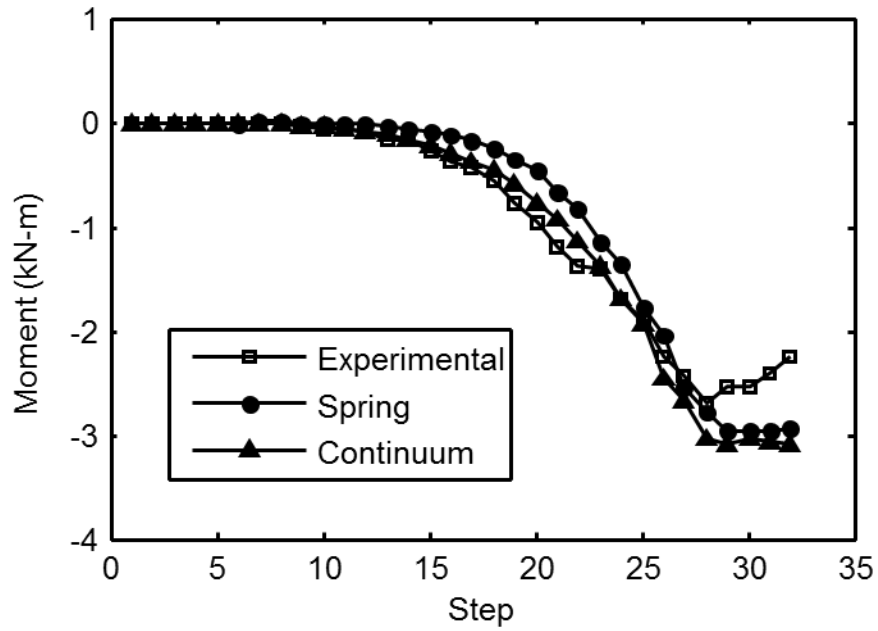
Figure 19. Tall Arch Apex Moment During Backfilling
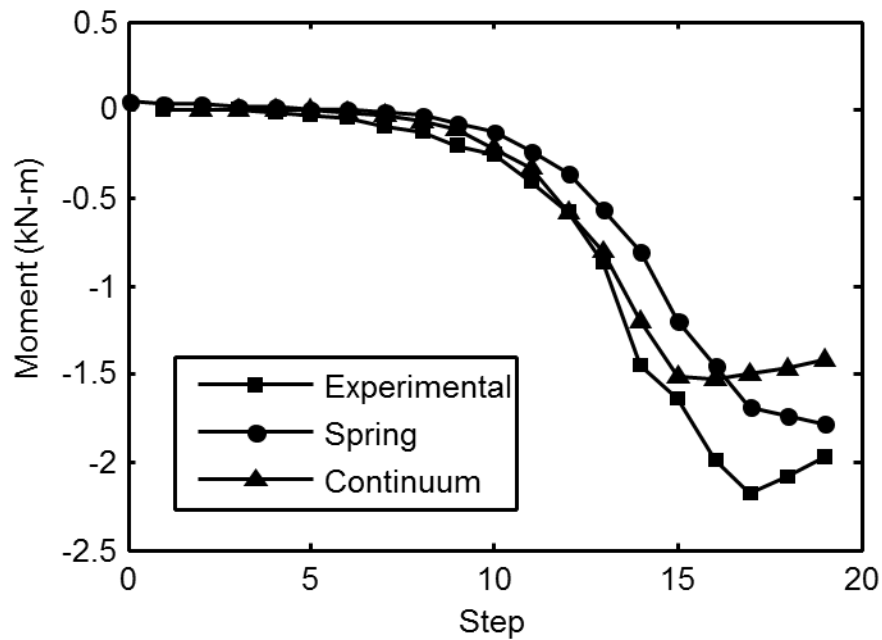
Figure 20. Short Arch Apex Moment During Backfilling

Figure 21 shows arch moments near the North footing of the tall bridge. The soil-continuum model and soil-spring model both do a poor job of predicting moment after step 22. The soil-continuum model continues to predict larger negative moment with each step instead of reducing in negative moment as shown by experimental data, overpredicting final footing moment by 200%. The soil-continuum model better predicts final moment, only over-predicting by 15%, but it over-predicts negative moment by a maximum of 65% at step 27. Most likely, the experimental arch foundation has greater rotation than predicted by the model because neither model accounts for the compressible plastic pads under the footing.

36
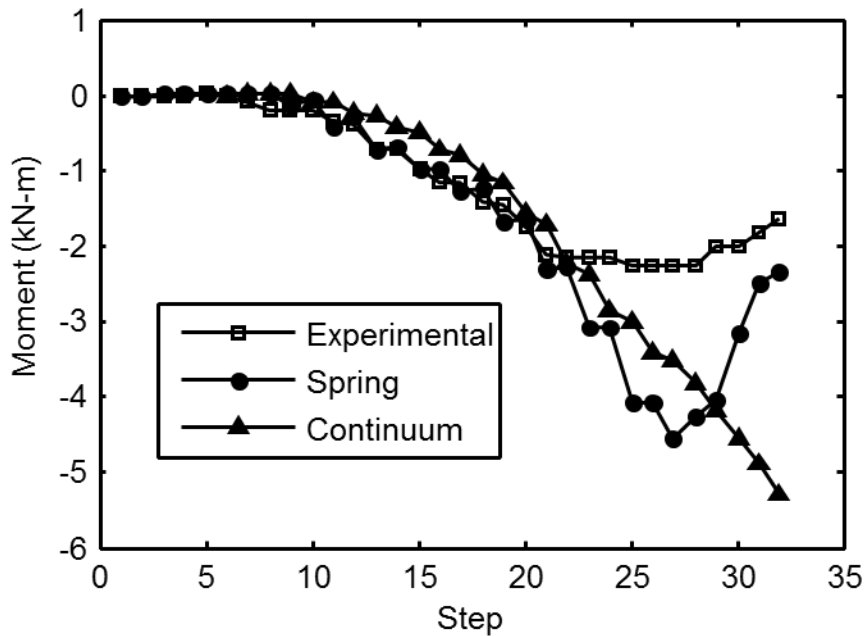
Figure 21. Tall Arch Foundation Moment During Backfilling

Figure 22 and Figure 23 show post-backfilling moments along the arch arc length for both models and experimental results for the two bridge geometries with compacted soil. Generally, moments predicted by both models follow a similar trend as the experimental moments, however apex moment magnitude is overpredicted by the soil-spring model by 27% for the tall bridge and 7% for the short bridge, while the soil-continuum model over-predicts the apex moment by 28% for the tall bridge and 27% for the short bridge. The models indicate peak positive moment appears near the span quarter points for the tall bridge and one-eighth of the span away from foundations for the short bridge. The soil-spring model predicts a more symmetric response than was experimentally observed, as illustrated by the overprediction of peak positive moment in the tall bridge by only 13% on the South side and 70% on the North side. The soil-continuum model also reports a smaller side to side difference than experimental results. The short bridge soil-spring model underpredicts the peak positive moment by 17% and predicts that the peak moment

37

is closer to the quarter point. Foundation moments are well represented by the soil-spring model with a difference of 20% or less compared to experimental results, and the model properly predicts asymmetric foundation moment response, but underpredicts the difference in magnitude. The soil-continuum model overpredicts foundation moments by as much as 220% and shows a need for further model refinement near the foundation.
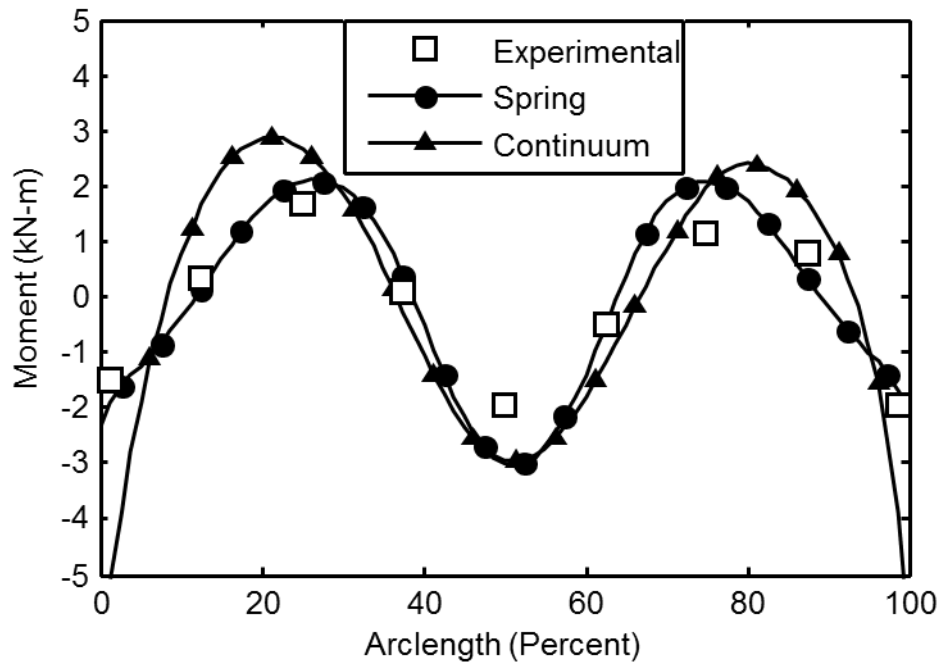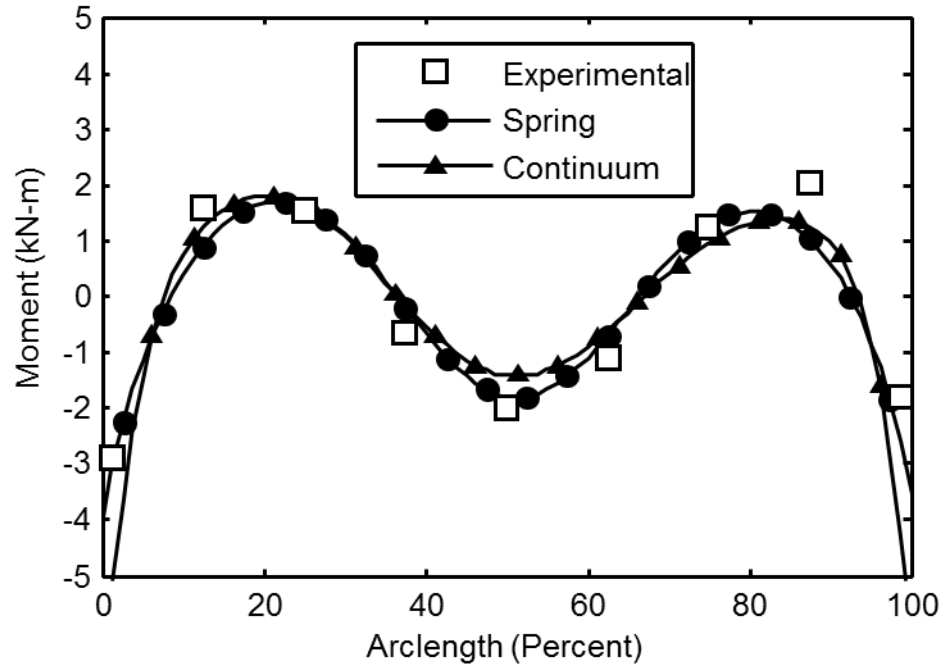
Figure 22. Moment at the End of Backfilling, Tall Bridge

Figure 23. Moment at the End of Backfilling, Short Bridge

We note that a simpler alternative to nonlinear soil-spring elements is to assume a constant lateral earth pressure coefficient K for all elements for all analyses. However, simulating backfilling with a constant K model proves challenging. This is particularly true for the tall bridge, where any K greater than 0.3 causes the arch to buckle as soil is applied up to the height of the arch apex. Apex moments in the tall arch exceed 11 kN-m, which are greater than experimentally-determined backfilling moments from Figure 19. In contrast, the soil-spring model having nonlinear soil springs allows K to drop to as low as 0.2 (nearly full-active) along more vertical elements between the apex and the foundation and also to exceed 2.0 at more horizontal elements between arch shoulders and the apex when the soil elevation is above the apex. The horizontal forces above the shoulder create positive moments and the horizontal forces below the shoulder produce negative moments, bringing the predicted arch moments closer to the

measured experimental data. This indicates the importance of accurately capturing soil pressures during the simulation of staged backfilling.

Live Load Response

The arches were loaded at intervals of 10% of the span between mid-span to 60% of the distance between the apex and the foundations. The steel arches remained elastic, with maximum measured total steel strains below 0.0013, or 75% of the yield strain. Peak displacements were 22 mm and 15 mm for the tall and short arches, respectively. Arch moments inferred from measured strains for the 83.4 kN service load are reported for each load position in Figure 24, Figure 25, Figure 26, Figure 27, Figure 28, Figure 29, Figure 30, and Figure 31. Total arch moment is inferred from measured strains including the strains in the current load test and the final strains from all previous live load and backfilling tests. Creep or relaxation between tests was not accounted for, and Figure 24, Figure 25, and Figure 26 show live load moment, which is the total moment less the moment at the end of backfilling
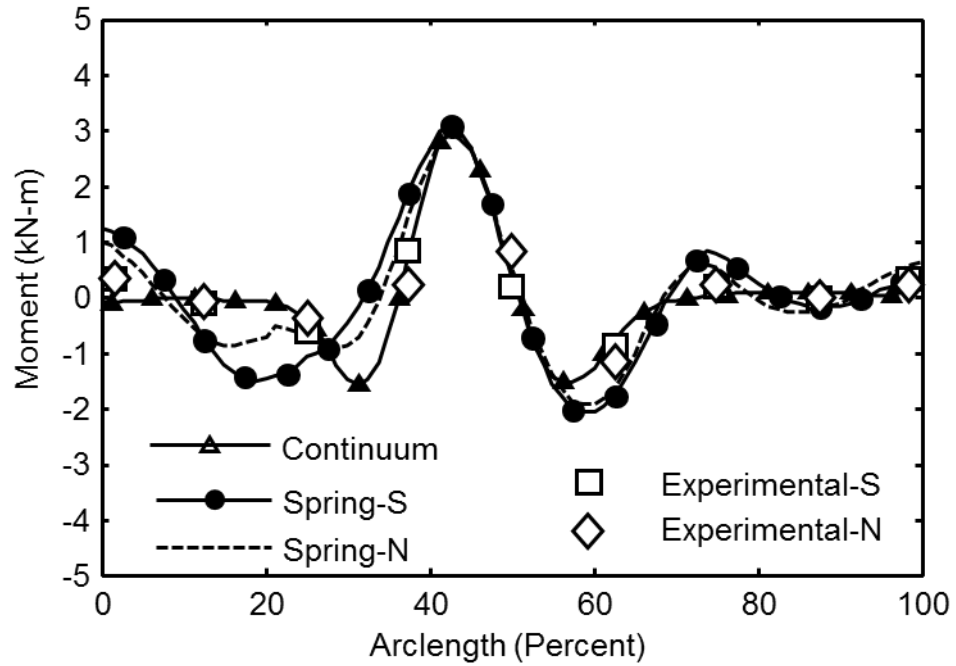
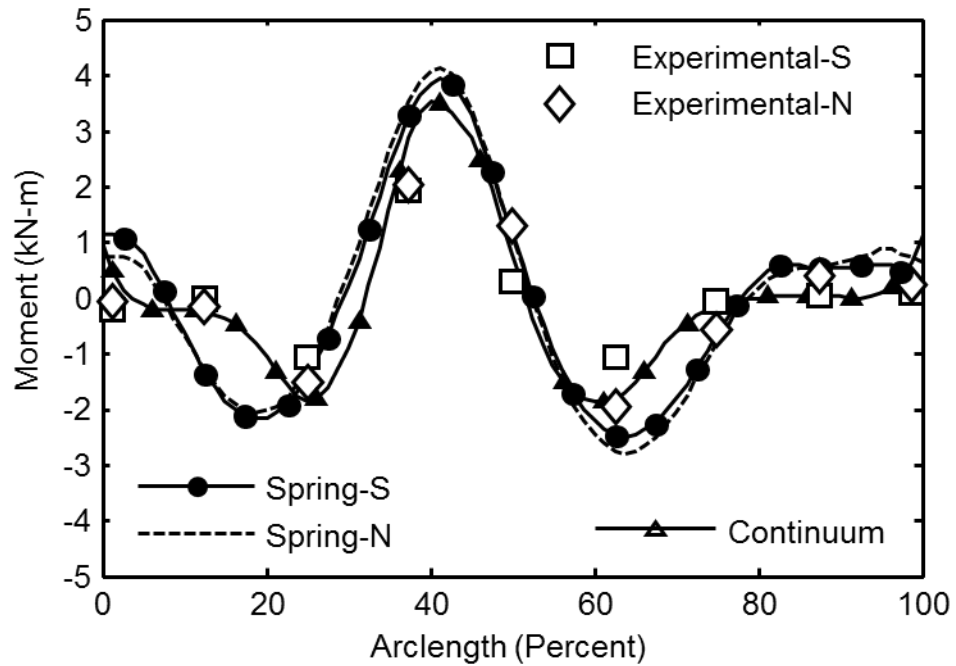Figure 24. 20% Offset Live Load Moment Diagram, Tall Bridge

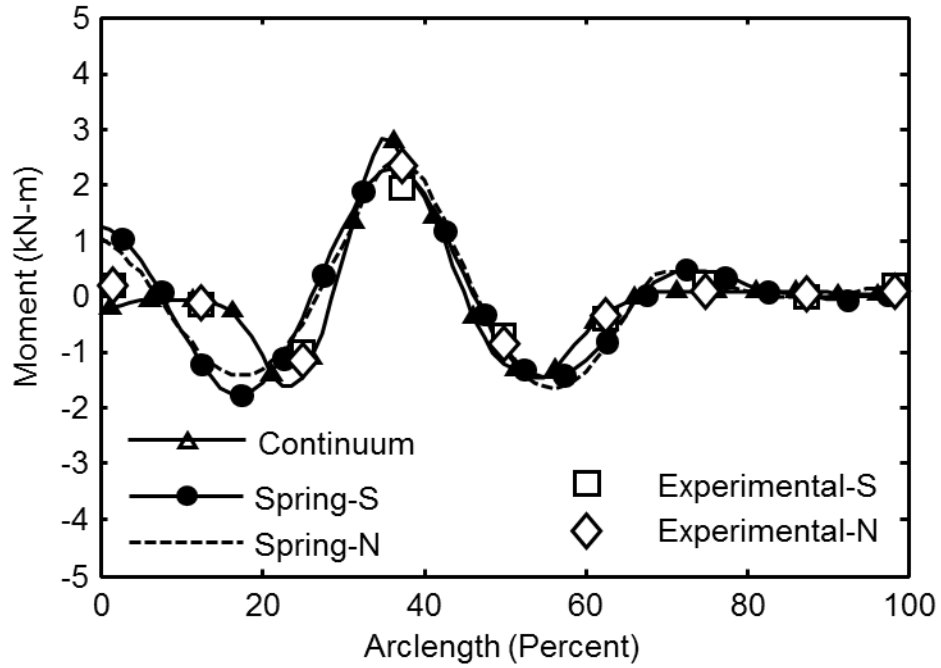Figure 25. 20% Offset Live Load Moment Diagram, Short Bridge

41

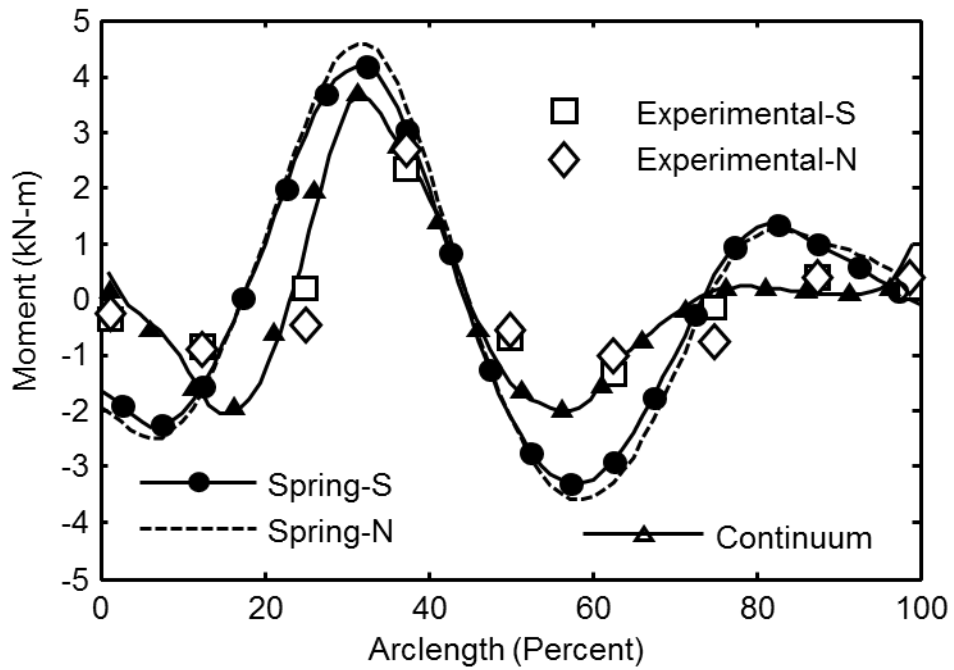Figure 26. 40% Offset Live Load Moment Diagram, Tall Bridge

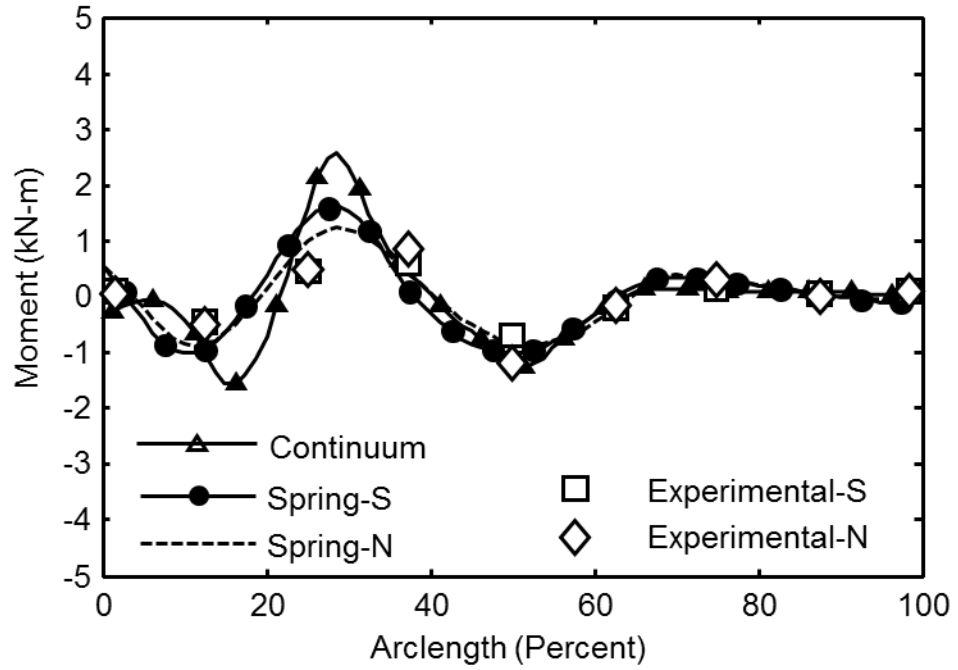Figure 27. 40% Offset Live Load Moment Diagram, Short Bridge

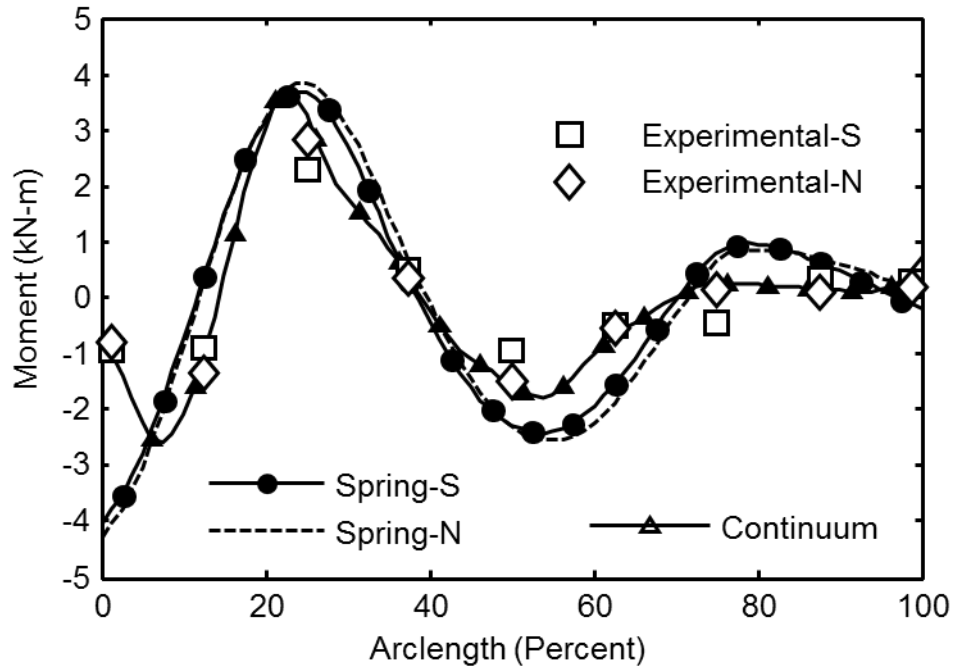Figure 28. 60% Offset Live Load Moment Diagram, Tall Bridge

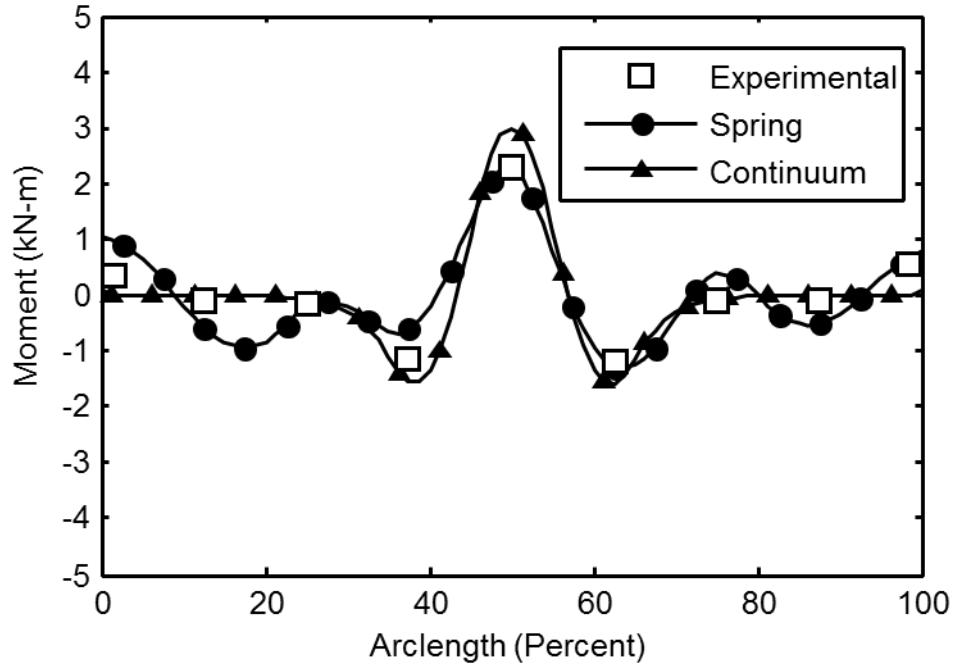Figure 29. 60% Offset Live Load Moment Diagram, Short Bridge

43

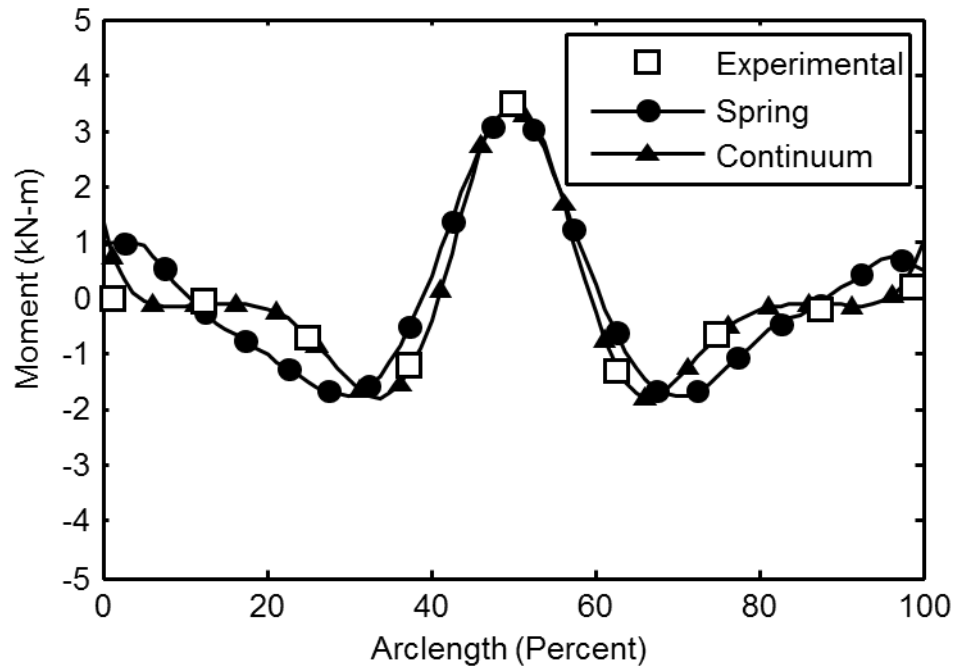Figure 30. Live Load Moment Diagram, Apex Load, Tall Bridge, with Models

Figure 31. Live Load Moment Diagram, Apex Load, Short Bridge, with Models

44

The response due to a North load and South load are reported on the same plot with the loaded side between 0% and 50% of span and the unloaded side between 50% and 100% of span. Experimental and soil-spring model predicted responses are not identical for each side; the soil-continuum model has nearly an identical response for both loading sides and the North side loading is omitted. Soil-spring model North and South results are similar, and differences are caused by the backfilling sequence that leads to locked-in displacement from spring initiation. Experimental results are additionally affected by live load history and soil densification that occurs following live load application and soil stresses increases. There is a more noticeable but still small difference in experimental results.

The soil-spring and soil-continuum models both produce acceptable design moments in many cases for peak positive moment. For the short bridge, peak positive moment differs by less than 10% between the two models for the three offset loading cases in Figures 25, 27, and 29. For the tall bridge, the soil-spring model predicts lower moments than does the soil-continuum model for Figures 24, 26, and 28, although the soil-spring model shows better agreement with the experimental results for a 40% offset load (Figure 26) and for apex loading (Figure 30). It is possible that the tall bridge is under-confined in the soil-continuum model, because the model assumes a constant soil elastic modulus with depth when in reality it increases with depth and overburden stresses. In contrast, the soil-spring model uses the vertical effective stress as a component of stiffness, thus allowing soil spring stiffness to increase with depth and change with deformation.

The soil-continuum model consistently tracked experimental moments away from the point of load application better than the soil-spring model. Practically, this does not affect the design of an arch bridge in most cases, because these moments do not control. The one exception where load away from the point load does control is negative moment at the foundation under the 60% offset

45

load for the short bridge (Figure 29). The experimental data shows nearly zero moment at the foundation and significant foundation rotation for this load condition. The soil-continuum model agrees with experimental data, predicting a greater foundation rotation that reduces the moment at the interface; the soil-spring model does not and is an indication of excessive foundation restraint.

Under 40% offset loading (Figure 26), gauges on the tall bridge coincide with location where peak positive moment was measured. Experimental data and soil-spring model predictions differ by less than 3% for North side loading and 11% for South side loading. The soil-continuum model agrees with the soil-spring model at the gauge location, however it predicts a 32% higher moment 5% of the arc length closer to the footing where there were no gauges. This indicates that for off-center loads, the tall bridge soil-spring model and soil-continuum model both predict the moment well where it can be verified. This cannot be verified for 20% and 60% offsets, however, because gauges did not correspond with peak moment locations.

Figure 30 and Figure 31 illustrate apex load moment response for the tall and short bridge. Apex moments are well captured by the soil-spring model, differing by 5% or less for both the tall and short bridge. The soil-continuum model predicts a very similar response for the short bridge, but overpredicts the apex moment response by 25% for the tall bridge. Moments distant from the apex also follow the predicted trend; however reported percent differences are deceptive due to the low magnitude of the experimental moments. Foundation moment magnitudes are over-predicted by the soil-spring model for both bridge geometries for every loading case. The soil-continuum model also over-predicts footing moments in many loading cases, but it adequately predicts footing moment in most live load applications and would never a design controlled by footing live load moment.

Apex live load produces positive foundation and apex moments, which oppose the negative backfilling moments. Therefore, apex loading may not be the worst case loading scenario for design. Results for live load in Figures 24 through 31, taken with the moments at the end of

backfilling given in Figure 22 and Figure 23, indicate that total positive moment is highest near the shoulders at positions 2 or 6 for a 60% offset load for both the tall and short bridge, and the peak negative moment is highest at the apex for the tall bridge or at the footing for the short bridge for a 60% offset load.

The live load moment soil-spring model predictions for the short arch are better for an apex load than for an offset load, and as the load is moved further from the apex, the soil-spring model increasingly over-predicts peak moments. Comparing Figure 29 (short bridge 60% offset) with Figure 31 (short bridge apex load), peak positive moment predicted by the soil-spring model for the apex load differs by 5% while peak positive moment at 60% offset differs by 30% to 45% (North or South loading). This difference is likely due to the Boussinesq load distribution assumed in the soil-spring model, which does not consider soil arching action and large restraint at the foundation. Further, the uncoupled horizontal soil springs are incapable of capturing the continuum response of the soil. Near the apex, soil arching is small since the soil cover above the arch is shallow. This is borne out by the soil-continuum model's somewhat better predictions of the peak positive moment, and substantially better prediction of the footing negative moment. As surface pressure is applied further from the apex, soil cover increases and soil arching action will have a more significant effect, spreading loads to adjacent soil as opposed to loading the arch. As surface pressure is distributed toward the foundation, moments decrease in the structure.

Figures 32, 33, and 34 include the experimental moments due to an apex live load for the short bridge, the tall bridge with compacted soil, and the tall bridge with under-compacted soil, respectively. The figures contain diagrams for virgin apex loading, the moment due to a third cycle of load, retesting with the same boundary conditions after completing the seven load positions, and with unrestrained foundations after removal of the tie-rods. The tall bridge was not retested to 83 kN, and that data set is omitted from Figure 33. The soil-spring model is elastic and

does not account for live load history; the soil-continuum model does not accurately represent

stored arch strains and as such the model results are omitted from Figures 32, 33 and 33.
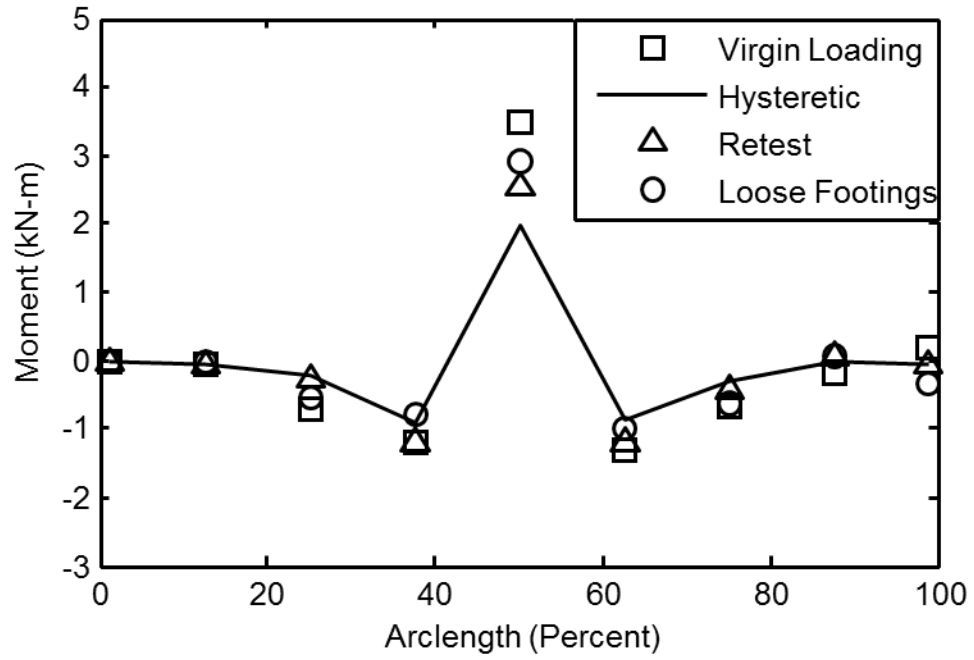

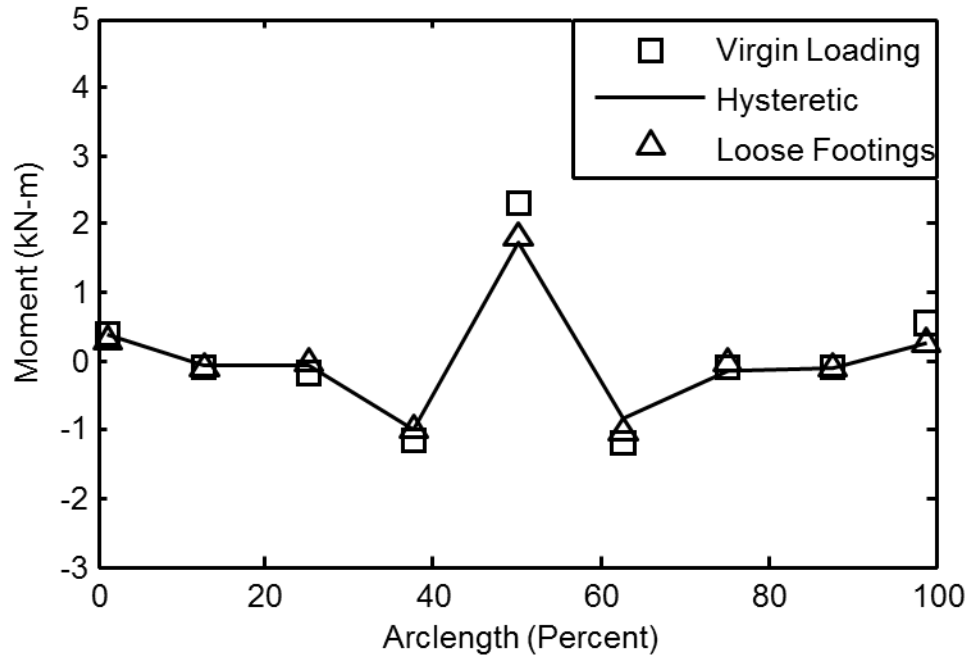Figure 32. Moment Diagram, Apex Live Load, Short Bridge

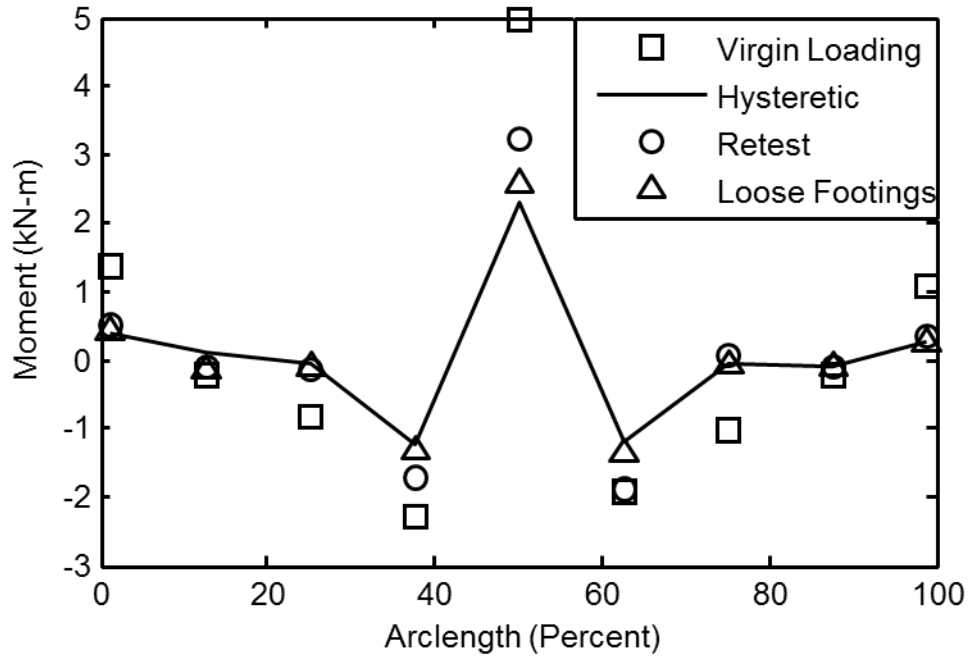Figure 33. Moment Diagram, Apex Live Load, Tall Bridge, Compacted Soil

Figure 34. Moment Diagram, Apex Live Load, Tall Bridge, Under-Compacted Soil

In all cases, the peak positive moment occurs directly under the point of load and the peak negative moment occurs one station to the North or South, not at the quarter points. The virgin peak positive moment is in all cases the highest moment. As the arch deforms under load it loads the soil, which results in locked-in stresses and deformations after load is removed from the structure. This effect diminishes with load cycling. Figure 35 includes the apex moment response for the short bridge for all three load cycles, which illustrates that there is less than 10% difference in the final moment between the first and third load iteration. However, the change in moment due to live load in the third cycle is only about 50% of the change in moment due to the initial live loading.
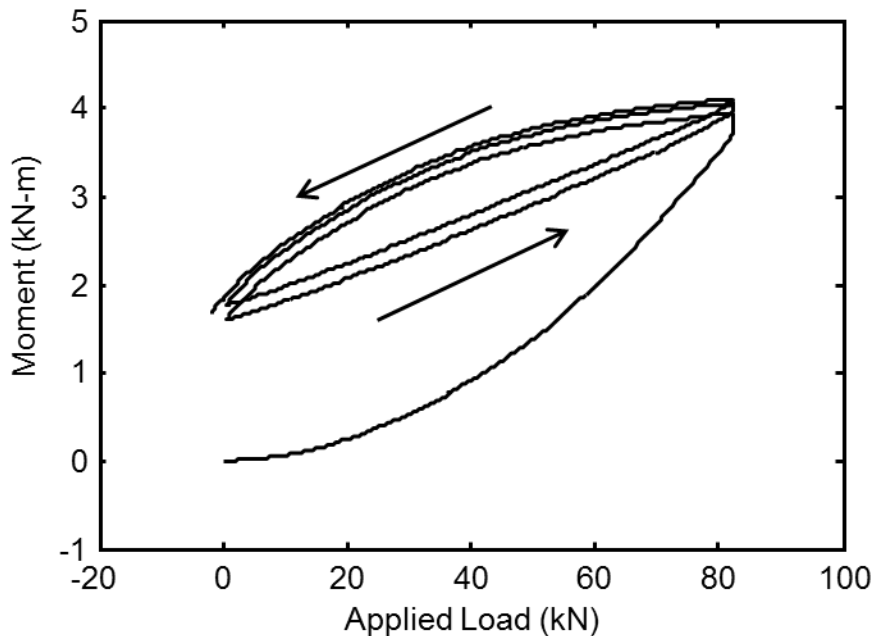

Figure 35. Middle Arch Apex Moment Response to Three Apex Load Cycles, Short Bridge

The effect of compaction is pronounced, especially for the virgin load. The peak apex moment for the virgin load is 115% greater for the under-compacted tall bridge than the

compacted tall bridge. Repeated loading has a smaller effect, likely because the soil densifies from live loading and better confines the arches and distributes subsequent live loadings. The under-compacted bridge third load apex moment is only 32% higher than the compacted bridge. This effect is also observed at the foundation, where the virgin South foundation moment is 150% higher and the virgin North foundation moment is 180% higher for the under-compacted bridge versus the compacted bridge. This is consistent with prior research; for example, McCavour (1998) tested buried plate arch bridges with backfill at 95% relative compaction and at 85% relative compaction bridge, and found a 50% difference in maximum apex moment due to vehicular live load. However, the tests performed here indicated that this difference quickly goes away under load cycling: the third load cycle response is the same at the foundations for the compacted and under-compacted cases. Compaction during construction helps confine the bridge reducing the initial live load moment and reducing the total measured moment in the bridge, allowing for a more efficient structure.

Arch Response and Soil Pressures during Ultimate Loading

Figure 36 through Figure 43 include results from ultimate load tests. Experimental, soil-spring model, and short bridge soil-continuum model system failure was in-plane symmetric buckling ("snap-through") for the steel arches. As observed experimentally, the tall bridge soil-continuum model predicts a soil bearing failure under the load application point, but the soil-continuum model is incapable of converging beyond this event. As mentioned previously, there was considerable soil bearing failure (430 mm) in the tall bridge with an actuator displacement of 590 mm. Measured apex final deflections are 130 mm for the tall bridge and 180 mm for the short bridge, although this is based on one gauge, as two of three gauges exceeded the maximum measureable deflection. Soil-spring predicted apex deflection exceeded 130 mm for the tall

51

bridge and 160 mm for the short bridge, showing good agreement with experimental results. Deflections are smaller for the soil-continuum model because it does not track post-buckled response. While arch apex moments are below the full plastic moment determined from coupon tension test data (17 to 19 kN-m), predicted and measured moments are both significantly above the moment at first yield, 8 to 9 kN-m. Experimental arch strains exceeded 0.06 at the apex of the tall bridge and 0.04 at the apex of the short bridge, which are much greater than the yield strain of 0.0018.

Figure 36 and Figure 37 illustrate the ultimate load total moment response for the tall and short bridges respectively. Experimental data include backfilling and hysteretic locked-in strains resulting from all prior loads. Notice the considerable difference in initial experimental apex moment for both plots compared to the apex moment at the end of backfilling (Figure 22 and Figure 23). The models only include backfilling, and match the previously presented model values. Live load sequence changes the moments locked in the arches, and future loads thus cause different response than initial loads. However, once the load exceeds the maximum previously applied load of 83.4 kN, the soil-spring model-predicted and experimentally-determined moments agree up to soil-spring model predicted arch failure.
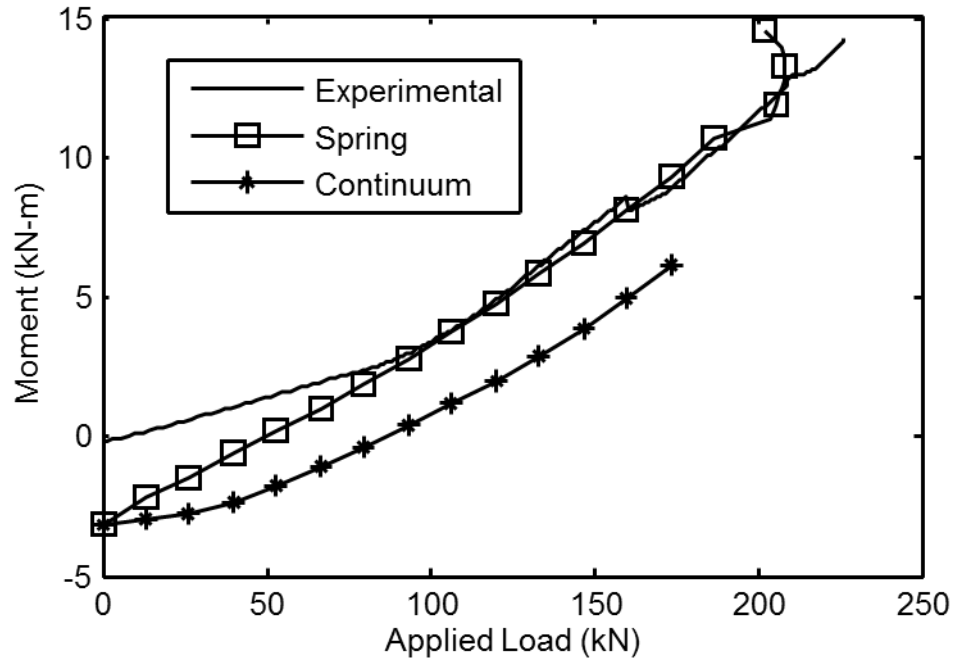
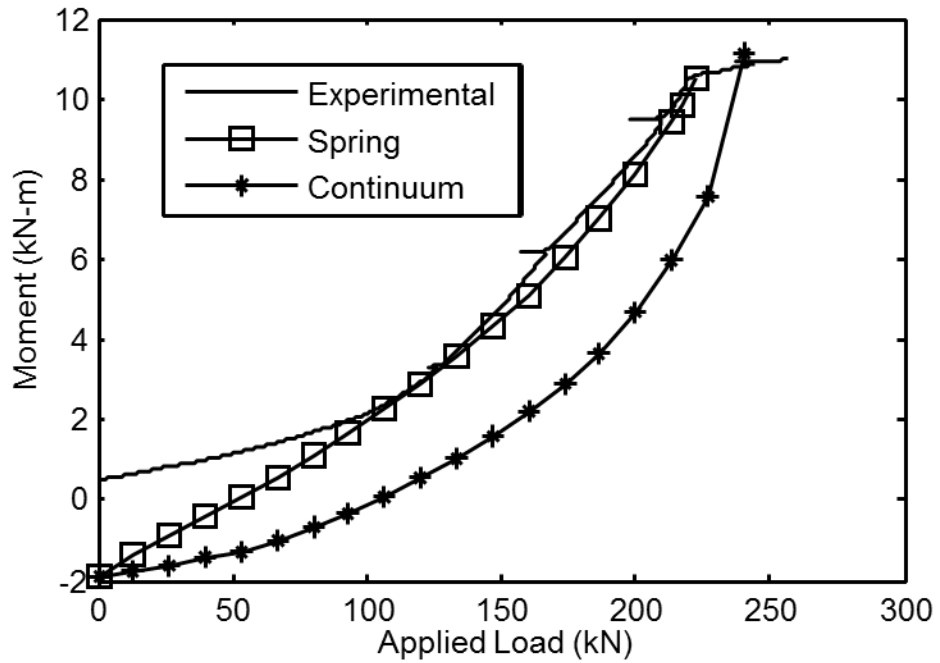Figure 36. Ultimate Total Moment, Apex Load, Tall Bridge

Figure 37. Ultimate Total Moment, Apex Load, Short Bridge

Soil arching action and load redistribution do not play a large role for much of ultimate loading given that the load is applied near the apex of the arch where soil cover is small. Near the end of ultimate loading apex deflections become large allowing soil arching despite the shallow cover. Experimental pressure for the short bridge diminished prior to ultimate load and for the tall bridge plateaued. This may explain the approximate 15% difference in capacity between experimental results and the soil-spring model, which does not redistribute live loads. The soil-continuum model predictions differ from the soil-spring model predictions, in that they do not approach the experimental results near the past peak load. The short bridge soil-continuum model predicts the buckling load within 6%, but this appears to be fortuitous as the model does not track moment response until it nears ultimate load.

The experimental moment agrees for all three arches in the system, thus an average experimental moment is used for clarity. During ultimate loading the arches yield at the apex and ultimate capacity is reached beyond the yield moment of the arches. The final deformed shape of the arches corresponded to a snap-through buckling of the arch, where the original downward apex curvature was inverted. The nearly constant moment for the final 40 kN of load shown in Figure 37 occurs after the short arches have yielded substantially. At this point there is only a small increase in moment with regard to strain, and the load distribution pad shown in Figure 4 allows load to spread away from the apex. The tall bridge apex moment (Figure 36) is also beyond yield, but because no distribution pad was used in this test the arches continue to strain and the moment continues to increase in the middle rather than being spread over a larger area.

Apex soil pressure and displacement results for the tall and short bridges are given in Figures 38 and 39. The large pressure difference between the tall and short bridges is a function of load application – the tall bridge is loaded over a 152 mm long strip, full width, which embeds 430 mm into the soil, while the short bridge is loaded over a larger 760 mm long strip, full width, which embedded less than 50 mm into the soil. The tall bridge apex TPC measures over 60% of

54

the actuator applied surface pressure. The short bridge apex TPC at failure measures a sharp

decrease in vertical apex soil pressure after about 140 kN of applied load, with a total pressure

below pressure at the start of the step. The larger distribution pad allows the load to spread away

from the apex when the arch deforms and the soil-arch contact pressure is higher away from the
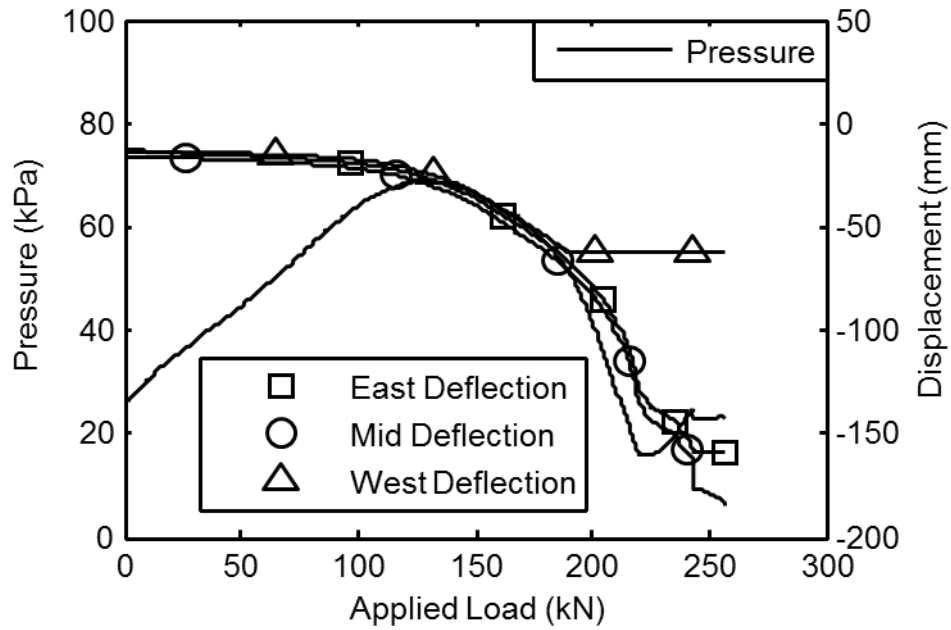
apex.

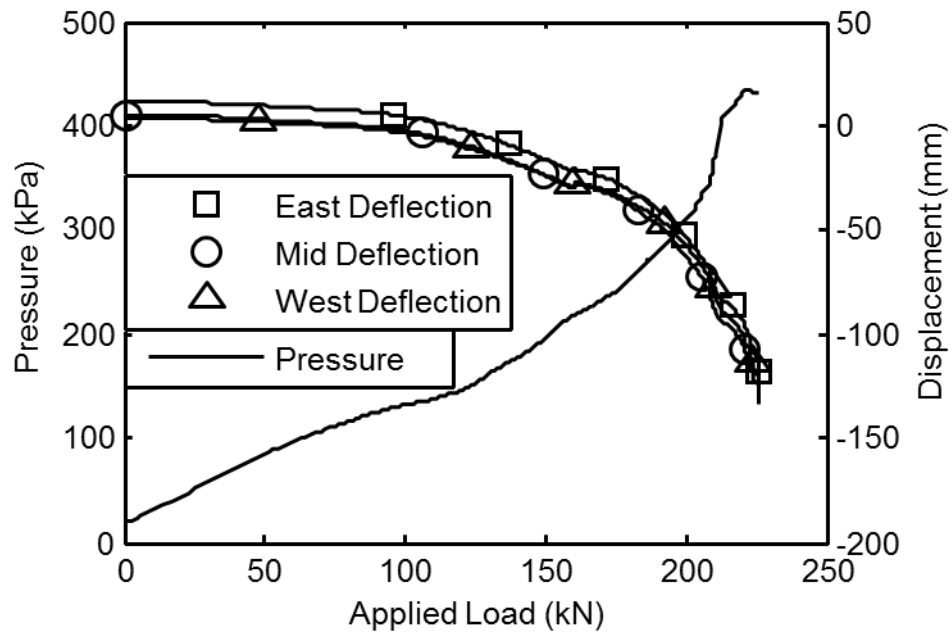Figure 38. Ultimate load apex pressure and deflection, short bridge

Figure 39. Ultimate load apex pressure and deflection, tall bridge

This is consistent with the soil pressures measured at the arch shoulders. Measured vertical pressure in the tall bridge at the shoulder (Figure 40 and Figure 41) is small compared to the horizontal pressure despite vertical displacements into the soil that are nearly 75% of the magnitude of horizontal displacements. In contrast, the short bridge (Figure 42 and Figure 43) sees higher vertical pressures than horizontal pressures at the shoulder despite negative (away from the soil) vertical displacements, indicating that vertical pressure response is influenced by load distribution, not vertical passive soil resistance.
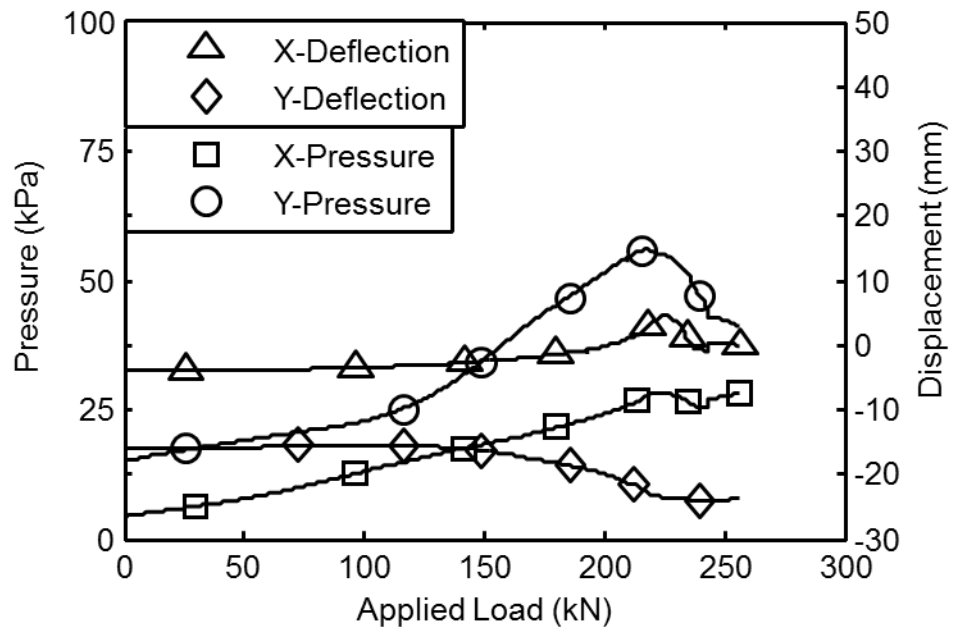
Figure 40. Ultimate Load South Shoulder Pressure and Deflection, Short Bridge
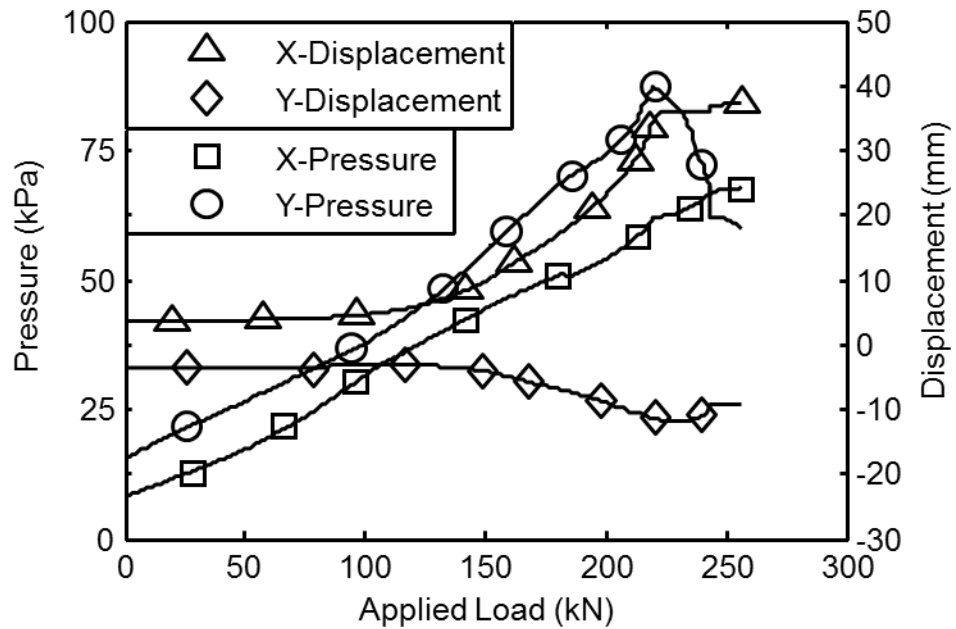

Figure 41. Ultimate Load North Shoulder Pressure and Deflection, Short Bridge
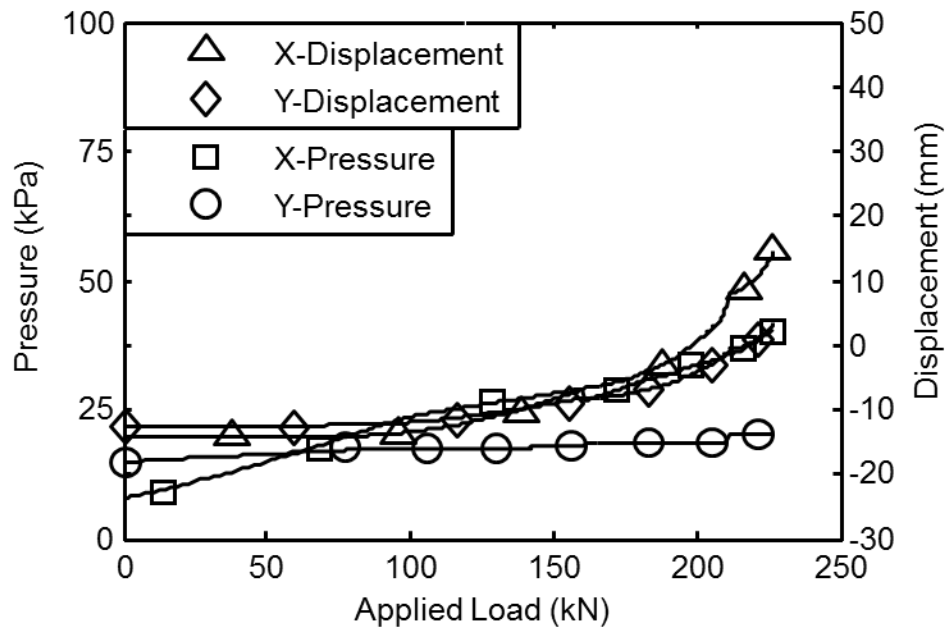
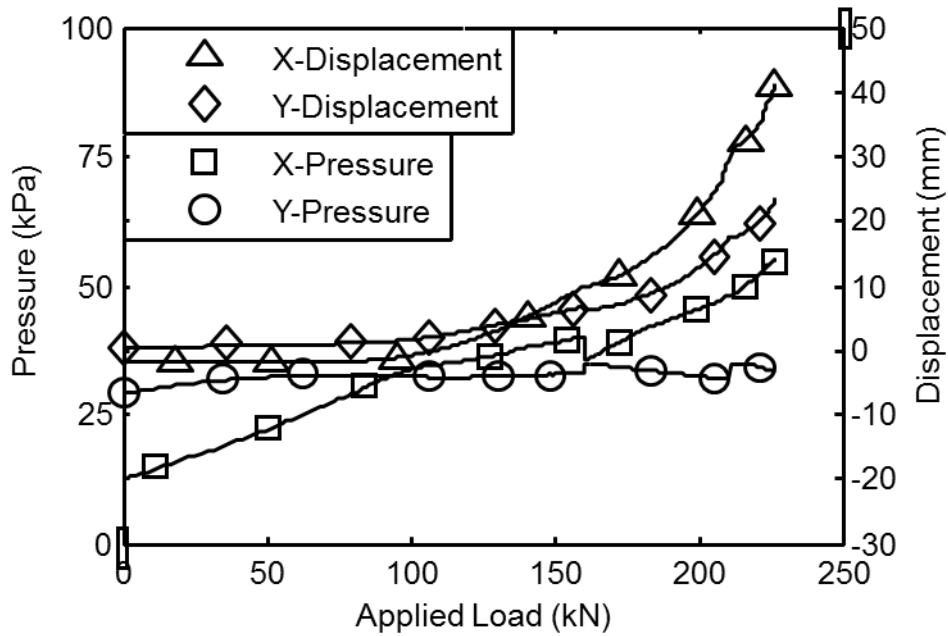Figure 42. Ultimate Load South Shoulder Pressure and Deflection, Tall Bridge

Figure 43. Ultimate Load North Shoulder Pressure and Deflection, Tall Bridge

The soil-spring model underpredicts the experimental ultimate load by about 15% for both the tall and short bridge, but remains an effective analysis tool compared to those with simpler soil assumptions. To demonstrate this, three simpler 2D models were created and used to predict ultimate capacity: a point loaded arch without soil, a point loaded arch with wished-in-place soil, and an arch with wished-in-place soil and assumed Boussinesq load distribution for an apex point load at the soil surface. The wished-in-place soil treated lateral soil loading assuming a deformation-independent fluid pressure with a horizontal earth pressure coefficient of 0.5. For all three models, arch capacity was limited by in-plane symmetric buckling of the arch, which corresponded to the actual failure mode.

Table 1. Buckling Load per Arch

Bridge	Tall (kN)	Short (kN)
Point Load, No Soil	33	37
Point Load, Dead Soil (K=0.5)	34	32
Boussinesq, Dead Soil (K=0.5)	35	45
Boussinesq, Springs	69	73
Experimental	78	86

Predicted capacities are given in Table 1. They indicate that, for both bridges, the soil-spring model better predicts the buckling load than simpler models that incorporate constant lateral earth pressure assumptions. The closest result of any model with wished-in-place soil has a predicted capacity of at most 52% of the measured capacity. Results in Table 1 indicate that models assuming a lateral earth pressure coefficient of 0.5 and ignoring lateral restraint provided by the soil predict only a small increase, or in one case a decrease, in arch ultimate capacity compared to a free-standing arch with no soil. Buried arches have greater capacity than free-standing arches

due to soil restraint, which is neglected in analyses using constant stiffness soil. Varying earth pressure coefficient with deflection allows an arch to go from the active and at-rest pressures typical at the end of backfilling to the passive pressures at ultimate load, which magnify the arch capacity and allow the model to predict a more realistic buckling load response, differing by 15% from experimental results rather than 50% or greater.

Conclusions

Two buried steel arch bridges were instrumented and tested during backfilling and under live loading. This report describes the testing and modeling efforts for these bridges in order to make comparisons between experimental data and model results from a soil-spring model and a soil-continuum model. The soil-spring model incorporates large-deformation analysis, horizontal non-linear elastic soil springs, and a Boussinesq distribution for surface loads. The soil-continuum model uses Mohr-Coulomb plasticity and frictional contact to distribute load from the soil mass to a beam element arch. Model results focus on moments while experimental data also includes displacements and soil pressures to get a more robust representation of soil-structure interaction. Experimental results also include the effects of soil compaction and repeated loading. Significant conclusions from this report are given below:

- Poor arch confinement resulting from under-compacted soil conditions produces higher moments in the arches during backfilling despite lower soil density.

- During initial live loading, bridges with under-compacted soil experience nearly twice the live load moments of bridges with compacted soil. This difference decreased with load cycling.

- Repeated loading does not substantially change the total arch moment due to a given live load. Measured changes are within 15% for three load cycles for peak positive moment.

60

- The arch moment generated from a load is influenced by prior loading; soil is densified and sheared and rearranged during loading and locks the arches into a new configuration when load is removed.

- Peak backfilling moments for a tall bridge do not occur at the end of backfilling, but occur when soil is near the arch apex. Additional soil causes positive moment at the foundations and apex reducing the peak values. In contrast, the short bridge experienced peak foundation moments at the end of backfilling.

- The critical location for arch design can be near the shoulder, not the apex, because backfilling moments are positive at the shoulder and live loads also produce positive moments for a surface load near the shoulder. In contrast, total moment at the apex is relatively small since the apex moment due to backfilling is negative while the maximum live load apex moment response is positive.

- The soil-spring model acceptably predicts backfilling moments. Foundation moments are predicted within 20% and apex moments are over predicted by the model by 32% and 10% for the tall and short bridge respectively.

- The soil-spring model acceptably predicts the apex moment from an apex live load.

- The soil-spring model is conservative in predicting peak positive moment for offset loads. The tall bridge model predicted moments are better than the short bridge, but the model is either conservative or within 5% of measured moments for all service live loads.

- Foundation live load moments are overpredicted by the soil-spring model, but backfilling foundation moments are acceptably predicted by the model. This may be caused by foundation restraint in the soil-spring model.

- Ultimate load capacity is better predicted by the soil-spring model than by simple models that neglect soil springs. The soil-spring model predicts arch buckling before full plastic moment, as experimentally determined.

61

- During ultimate loading the soil-spring model acceptably predicts the moment from the maximum previously applied load until the model predicted buckling load. This shows that the model is capable of predicting response due to an overload vehicle.

- While the soil-continuum model better tracks moments away from the point of loading due to its ability to capture soil arching action and better predict the live load stress distribution, these moments typically do not control arch design.

- The soil-continuum model overpredicts final backfilling foundation moments and does not follow the same trend as experimental data and soil-spring model results for backfilling moments.

There are several improvements that could further enhance soil-spring model performance and reduce conservatism. as outlined below:

- **Optimize Soil Spring Direction.** The soil-spring model uses horizontal soil springs, which may not be realistic near the shoulders and apex where the arch becomes nearly horizontal itself. Because the spring tributary area is small in these regions, the model may underestimate the confining properties of the soil on top of the arch. Further study considering radial or friction angle springs (with limits when the soil cover is too shallow) may provide more realistic pressure response near the shoulders of the arch.

- **Improved Live Load Distribution.** The Boussinesq load distribution assumption is adequate when load is applied at the apex, but is not as the load is applied closer to the foundations. The load distribution model is not arch deflection dependent. A coupled continuum-beam model could solve this problem or potentially an analytical expression for vertical pressure magnification as a function of relative arch movement.

- **Soil Hysteresis.** While the soil-spring model as presented uses elastic soil springs and is therefore unable to store the effects of soil compaction from live loads, load history changes the response of the real structure. Including the ability of the soil springs to store

load history would likely improve model predictions, although it may have limited value
for routine design.

References

AASHTO. (2012). LRFD guide specification for design of concrete-filled FRP tubes, 1st ed., AASHTO, Washington D.C.

AASHTO. (2014). *LRFD Bridge design specifications,* 7th Ed., AASHTO, Washington D.C.

ABAQUS, (2011) `ABAQUS Documentation', Dassault Systèmes, Providence, RI, USA.

ASTM Standard A309, (2014), "Standard test method and definitions for mechanical testing of steel products." ASTM International, West Conshohocken, PA, DOI:10.1520/A0370-14.

ASTM Standard A370, (2014), "Standard test method and definitions for mechanical testing of steel products." ASTM International, West Conshohocken, PA, DOI:10.1520/A0370-14.

ASTM Standard D698-07, (2007), "Standard test methods for laboratory compaction characteristics of soil using standard effort." ASTM International, West Conshohocken, PA, DOI:10.1520/D0698-07E01.

ASTM Standard D1556-07, (2007), "Standard test method for density and unit weight of soil in place by sand-cone method." ASTM International, West Conshohocken, PA, DOI:10.1520/D1556-07.

ASTM Standard D3080-11, (2011), "Standard test methods for direct shear test of soils under consolidated drained conditions." ASTM International, West Conshohocken, PA, DOI:10.1520/D3080_D3080M-11.

Ates, S., Constantinou, M. C. (2011). "Example of application of response spectrum analyses for seismically isolated curved bridges including soil-foundation effects." *Soil Dynamics and Earthquake Engineering*, 31, 648-661.

Barker, R.M., Duncan, J.M., Rojiani, K.B., Ooi, P.S.K., Tan, C.K., Kim, S.G. (1991). "*NCHRP 343: Manuals for the design of bridge foundations*." Transportation Research Board, Washington D.C.

Bayoglu Flener, E. (2009). "Response of long-span box type soil-steel composite structures during ultimate loading tests." *Journal of Bridge Engineering*, 14, 496-506.

Bayoglu Flener, E. (2010a). "Testing the response of box-type soil-steel structures under static service loads." *Journal of Bridge Engineering*, 15, 90-97.

Bayoglu Flener, E. (2010b). "Soil-steel interaction of long-span box culverts – performance during backfilling." *Journal of Geotechnical and Geoenvironmental Engineering*, 823-832.

Chung, J., Patil, A., Bollmann, H. (2011). *FB-Multipier API soil Model Validation*. Bridge Software Institute, Gainesville, FL.

Clough, G.W., Duncan, J.M. (1990). "Earth pressures." *Foundation Engineering Handbook*, 2nd ed., editor: Fang H.S., Van Nostrand Reinhold, Norwell MA, 224-235.

Crisfield, M.A. (1991). Non-linear finite element analysis of solids and structures, volume 1, Wiley, Chichester.

Dagher, H.J., Bannon D.J., Davids, W.G., Lopez-Anido, R.A., Nagy, E., Goslin, K. (2012). "Bending behavior of concrete-filled tubular FRP arches for bridge structures." *Construction and Building Materials*, 37, 432-439.

Davids, W.G., Walton, H.J., Clapp, J.D., Lopez-Anido, R., Goslin, K. and Dagher, H.J. (2012). "Response of Concrete-Filled Tubular FRP Arches to Construction-Induced Loading." *Proceedings of the 2012 International Bridge Conference*, Pittsburgh, PA, June 2012.

Demkowicz, M. (2011). "Environmental Durability of Hybrid Braided Polymer Matrix Composites for Infrastructure Applications." MS Thesis, Department of Civil and Environmental Engineering, University of Maine.

Drnevich, V.P., Evans, A.C., Prochaska, A.B. (2007). "A study of effective soil compaction control of granular soils." *Publication FHWA/IN/JTRP-2007/12*. Joint transportation research program, Indiana Department of Transportation and Purdue University, West Lafayette, Indiana.

Elshimi, T.M., Brachman, R.W.I., Moore, I.D. (2014). "Effect of truck position and multiple truck loading on response of long-span metal culverts." *Canadian Geotechnical Journal,* 51, 196-207.

Greimann, L.F., Yang, P-S., Wolde-Tinsae, A.M., (1986). "Nonlinear Analysis of Integral Abutment Bridges." J. Struct. Eng., 5(1), 1-10.

Holtz, R.D., Kovacs, W.D. (1981) *An Introduction to Geotechnical Engineering*, Prentice Hall, Upper Saddle River, New Jersey.

Jeong, S., Seo, D. (2004). "Analysis of tieback walls using proposed P-y curves for coupled soil springs." *Computers and Geotechnics*, 31, 443-456.

Kang, J., Parker, F., Yoo, C.H., (2008). "Soil-structure interaction for deeply buried corrugated steel pipes Part I: Embankment installation." *Engineering Structures*, 30, 384-392.

Lehane, B.M., Keogh, D.L., O'Brien, E.J. (1999). "Simplified elastic model for restraining effects of backfill soil on integral bridges." *Computers and Structures*, 73, 303-313.

Mak, A.C., Brachman, R.W.I., Moore, I.D. (2009). "Measured response of a deeply corrugated box culvert to three-dimensional surface loads." In *Proceedings of the Transportation Research Board Annual Conference,* Washington D.C.

MATLAB (2011), *MATLAB R2011b 7.13.0.564,* The MathWorks Inc., Natick, Massachusetts.

McCavour, T.C., Byrne, P.M., and Morrison, T.D. (1998). "Long-span reinforced steel box culverts." *Transportation Research Record,* 1624, 184-195.

Moore, I.D. and Taleb, B. (1999). "Metal culvert response to live loading: performance of three-dimensional analysis." *Transportation Research Record*, 1656, 25-36.

Morrison T.D. (2000). "Long-span deep-corrugated structural plate arches with encased-concrete composite ribs." *Transportation Research Record,* 1736, 81-93.

NAVFAC (1986), *DM 7.02 Foundations and Earth Structures*, Naval Facilities Engineering Command, Alexandria, Virginia.

Quinn, B.H., Civjan, S.A., Lahovich, A., Brena, S.F., Elnahal, S. (2013). "Monitoring of the first 'bridge-in-a-backpack' bridge in Massachusetts." Paper presented at *TRB 2013 Annual Meeting,* Washington D.C.

Petersen, D.L., Nelson, C.R., Li, G., McGrath, T.J., Kitane, Y. (2010). "*NCHRP 647: Recommended design specifications for live load distribution of buried structures*. Transportation Research Board, Washington DC.

Reese L. C. and Wang S.-T. (2006). "Verification of computer program *LPILE* as a valid tool for design of a single pile under lateral loading." www.ensoftinc.com.

SoilStructure.com (2013). Lateral Foundation v2.0 Software.

Taleb, B. and Moore, I.D. (1999). "Metal culvert response to earth loading: performance of two-dimensional analysis." *Transportation Research Record*, 1656, 25-36.

Vaslestad, J., Madaj, A., Janusz, L. (2002). "Field measurement of long-span corrugated steel culvert replacing corroded concrete bridge." *Transportation Research Record*, 1814, 164-170.

Webb, M.C., Selig, E.T., Sussman, J.A., McGrath, T.J. (1999). "Field tests of a large-span metal culvert." *Transportation Research Record*, 1656, 14-24.